Applied Thermal Engineering 220 (2023) 119797

Contents lists available at ScienceDirect

Applied Thermal Engineering

journal homepage: www.elsevier.com/locate/apthermeng

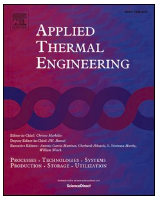

Research Paper

Global structural optimization of annular thermoelectric generators based on a dual-finite-element multiphysical model

Wenlong Yang [a], WenChao Zhu [a,b,*], Yang Li [a], Changjun Xie [a,b,*], Binyu Xiong [a], Ying Shi [a], Wei Lin [a]

[a] School of Automation, Wuhan University of Technology, Wuhan 430070, China
[b] Hubei Key Laboratory of Advanced Technology for Automotive Components, Wuhan University of Technology, Wuhan 430070, China

ARTICLE INFO

Keywords:
Annular thermoelectric generator
Structural optimization
Heat recovery
Heat transfer enhancement
Analytical solution

ABSTRACT

The conventional methods to improve the performance of annular thermoelectric generators (ATEGs) heavily rely on optimizing the thermal design of individual annular thermoelectric couples (ATECs). However, since a practical ATEG consists of many ATECs, the optimal structure of the ATEG can differ from the ATEC-based design. On the other hand, optimization by simply considering all ATECs can lead to a heavy computation burden. This work first proposes a high-fidelity, fluid-thermal-electric multiphysical ATEG model, solved by a computationally-efficient dual-finite-element method to cope with the challenge. This model explores the effects of ATEC microstructure and heat exchanger structure on ATEG performance under various operating conditions. Comparative multi-objective optimization studies were performed at three levels, i.e., for a single ATEC, a single ring of ATEG, and the entire ATEG. The results reveal that the optimized structural parameters of ATECs have some new features when considering the entire ATEG as the optimization objective. The optimal height, angle, and thickness of ATECs are 12 mm, 2.35°, and 10 mm, respectively. The corresponding net power, efficiency, and power density of ATEG are 321.6 W, 6.58 %, and 634.15 W/m^3, respectively. Compared to the traditional design method based on a single ATEC and a single ring, the net power of the ATEG designed with the proposed method can be enhanced by 168 % and 197 %, respectively, at the expense of only a 20 % reduction in the power density.

1. Introduction

The development of fossil-fuel-based energy systems has caused significant environmental and economic issues regarding climate change and air pollution, leading to soaring energy costs in recent years. The goal to reduce greenhouse gas emissions from fossil fuels and stop global warming has been established in different countries. The paradigm shift in the transport sector is majorly achieved by promoting electrified vehicles and improving traditional internal-combustion-engine-based vehicles using cleaner and renewable fuels [1]. In a typical fuel-powered vehicle, roughly 70 % of its energy consumption is wasted as heat, of which 40 % is discharged through the automobile exhaust system. Different thermal energy recovery technologies, such as those based on the Kalina cycle [2,3], thermophotovoltaic [4], organic Rankine cycle [5], and thermoelectric power generation [6–9], have been proposed. Among these technologies, directly converting heat into electricity using thermoelectric generators (TEGs) is a simple and environmentally friendly solution. Miniaturization, low noise, and no moving parts are among the benefits of TEGs. Recovering thermal energy from exhaust gas based on thermoelectric effects can also enhance fuel efficiency while meeting the industry standards on exhaust emissions [10]. Several pilot TEG projects for vehicle applications have been reported in recent years [11,12]. Nevertheless, the performance of the automobile TEGs is still far from being commercially viable.

A TEG usually consists of a large number of thermoelectric couples (TECs), and conventional TECs have a flat structure. However, since the vehicle exhaust duct is a cylindrical heat source, fitting such flat-type TECs (FTECs) into the vehicle system can lead to high contact thermal resistance and heat loss. This defect motivates the recent investigation of annular thermoelectric couples (ATECs). Such ATECs are also well suited for flexible micro-light-emitting diodes [13], annular solar thermoelectric generators [14], and liquefied natural gas cold energy recovery [15], where the heat sources are also cylindrical.

Due to the significant structural differences, conclusions of the studies for FTECs cannot be generally extensible and applicable to ATECs. Many research works have thus focused on ATECs and ATEGs in recent years. For example, Shen et al. [16] derived a set of fundamental

---

* Corresponding authors.
E-mail addresses: zhuwenchao@whut.edu.cn (W. Zhu), jackxie@whut.edu.cn (C. Xie).

https://doi.org/10.1016/j.applthermaleng.2022.119797
Received 30 June 2022; Received in revised form 30 September 2022; Accepted 30 November 2022
Available online 5 December 2022

Nomenclature

A	heat transfer area, m^2
c	specific heat capacity, J/(g•K)
D	diameter of heat exchanger, m
f_z	friction coefficient
F	Darcy resistance coefficient
h	convective heat transfer coefficient, W/(m^2•K)
H	thermoelectric leg height, m
H_r	surface roughness, m
I	loop current, A
k	total heat transfer coefficient, W/(m^2•K)
K	thermal conductance, W/K
L	length of heat exchanger, m
m	mass flow rate, g/s
n	the ring number
Nu	Nusselt number
P	output power, W
PD_V	Volumetric power density, W/m^3
Δp	pressure drop, Pa
Pr	Prandtl number
q	number of thermocouples in a single ring
Q	heat flow, W
r	radius, m
R	electric resistance, Ω
Re	Reynolds number
T	temperature, K
v	velocity, m/s
V_{oc}	Seebeck voltage, V

Superscript

i	index of a computational unit, i = 1, 2, ⋯, m
j	index of a computational unit, j = 1, 2, ⋯, n

Greek

α	the Seebeck coefficient, V/K
γ	dimensionless diameter
δ	thickness of thermoelectric legs, m
η	efficiency, %
θ	angle of thermoelectric legs, °
λ	thermal conductivity, W/(m•K)
μ	dynamic viscosity, Pa•s
ρ	resistivity, Ω•m
ω	density, kg/m^3
φ	angle of the gap between legs, °

Subscript

c	cold end of the semiconductor legs
cer	ceramic plate
cu	copper sheet
f	thermal fluid
h	hot end of the semiconductor legs
hex	hot side heat exchanger
i	inner cylinder of heat exchanger
$loss$	consumed pump value
L	external load
n	n-type semiconductor leg
net	net value
out	output value
p	p-type semiconductor leg
w	cold fluid/water

Abbreviations

ATEC	annular thermoelectric couple
ATEG	annular thermoelectric generator
FTEG	flat thermoelectric generator
TEG	thermoelectric generator

equations for an ATEC. They investigated the effect of the shape factor s_r on the thermoelectric performance under various load and temperature conditions. Subsequently, the same authors investigated the effect of ATEC shape parameters under constant heat flux conditions [17]. It was found that the higher the heat flux is, the better the performance the ATEC can have. It also showed that the ATEC outperformed the FTEC because unnecessary contact thermal resistance was reduced. Zhang et al. established a generic mathematical model to study the impacts of different design factors on thermoelectric properties. These factors include the dimension [18], contact resistance [18], and interfacial layer [19]. It was found that the interfacial layer in the ATEC would significantly degrade the performance of the ATEG. In order to obtain the best geometry with high thermoelectric and mechanical properties, Fan et al. [20] developed a numerical model for a single-ring ATEC. The authors investigated the effects of geometry and the number of ATECs in a single ring on thermoelectric performance and mechanical reliability. Asaadi et al. [21] established a three-dimensional (3D) transient numerical model of an ATEC where the effect of pulsing thermal input on thermoelectric properties is explored. Sun et al. [22] proposed an analytical model of ATEC that considers the Thomson effect. This model can be used to calculate ATEC power and efficiency conveniently. Tan et al. [23] proposed a numerical model of ATEC considering the interfacial layer. They found that the impedance of the interfacial layer leads to temperature drop and performance degradation while increasing the height of the ATECs can effectively improve the output power. Gao et al. [24] exhibited the influence of structural parameters of the thermoelectric legs and pulse currents on the cooling performance by developing a 3D transient model. Zaher et al. [25] proposed a dimensionless design factor that combines the diameter, filling ratio, and thickness ratio to obtain an optimal design parameter for maximum power output. Weng et al. [26] proposed a variable-angle ATEC to increase the output power and the maximum thermal stress on the semiconductor legs. The variable-angle ATEC they designed could increase output performance by 35 % but at the cost of a 30 % increase in maximum thermal stress on the thermoelectric legs.

In recent years, thermoelectric materials have made remarkable developments. Considering the different optimal temperature ranges of various thermoelectric materials, the segmented ATEC (SATEC) and the two-stage ATEC, where different thermoelectric materials are used in an annular thermocouple, have been proposed. Fan et al. [27] studied the thermoelectric performance and mechanical reliability of a SATEC in steady and transient states. The effect of structural parameters on the optimal thermoelectric performance was also presented. Shittu et al. [28] proposed a 3D finite element numerical model of SATEC, with which the effects of different geometries on optimal thermoelectric performance and thermal stress were studied. Asaadi et al. [29] investigated the thermodynamic performance and the exergoeconomic properties of two-stage ATECs. Their results showed that an angle ratio of one provided improved exergoeconomic performance and the minimum cost per output power. Tian et al. [30] examined the exergetic and economic performance of SATECs and discovered that the segmented structure outperforms the non-segmented one. Aljaghtham et al. [31] proposed a unileg segmented ATEC that can reduce thermal stress while increasing power generation capacity and efficiency.

In view of the above, there is plenty of research on single ATEC or single-ring ATECs. Nevertheless, from the perspective of an ATEG system, there can be a significant temperature difference between the thermal fluid and the cold end of the thermoelectric components.

Therefore, the optimal performance of an ATEG system cannot be guaranteed by ignoring this difference. A practical method to increase the power generation capacity and thermal energy recovery is improving the convective heat exchange between the exhaust and the thermoelectric components. At the same time, a significant temperature drop can be observed during the exhaust gas flow from the inlet to the outlet of the TEG, particularly in the cylindrical channel. Therefore, improving temperature uniformity over the entire TEG can significantly improve output performance and equipment life. The temperature uniformity inside a conventional FTEG is usually improved by filling with thermally conductive copper foam, spoiler tape, fins, and phase change materials. Some methods have also been proposed to improve heat transfer in ATEGs. For instance, Cui et al. [32] proposed a porous ATEG and studied the effects of gas flow rate, external resistance, and porosity on thermoelectric properties. They found that the porous structure increased the output power significantly. Tian et al. [33] studied the performance of annular thermoelectric coolers based on the heat transfer rate, temperature distribution, and other conditions of the thermoelectric legs. It was found that the annular thermoelectric cooler can be effectively used for cooling if the proper geometry is chosen. Yang et al. [34] suggested using a heat exchanger with a concentric annular channel to improve heat transfer inside the ATEG, resulting in higher power output and net power. Yang et al. [35] proposed a net power ratio metric to assess the impact of various heat transfer enhancement methods on power generation capacity. Furthermore, Huang et al. [36] investigated the effect of heat source parameters and cooling medium flow rate on the performance of ATEG.

Notably, due to the high processing/fabrication costs of thermoelectric elements, most researchers currently use a theoretical modeling approach to structurally optimize the parameters of a specific ATEG design without considering various geometric structures and comparing their performances with experimental and testing results. As seen from the summary of ATEC/ATEG models in Table 1, these theoretical models include numerical computational models, equivalent thermal resistance network models, and computational fluid dynamics (CFD) models. They have been used widely to simulate and optimize the performance of ATEGs in recent years.

From the above review of relevant literature, the structural optimization can be designed at three levels: 1) a single ATEC [16–19,21–24]; 2) a single ring of the ATEG [20,38]; and 3) the whole ATEG [33–36]. Schematic diagrams of the models for these three levels are shown in Fig. 1. The majority of the existing studies are for structural optimization of a single ATEC, as shown in Fig. 1(a), or an annular thermoelectric module or ring consisting of many ATECs connected in series, as shown in Fig. 1(b). However, a practical ATEG usually consists of hundreds of ATECs connected in series in the form of many rings to supply-one load (see Fig. 1(c)). Due to the coupling effect, the geometry optimization results of a single ATEC might not be applicable to the integrated ATEG with many ATECs, and thus we focus on the ATEG system as in Fig. 1(c) in this work.

Besides the theoretical models, three-dimensional (3D) ATEC finite element models built in multiphysics simulation software such as COMSOL or ANSYS can accurately predict the detailed distribution of thermoelectric properties and physical parameters of thermoelectric components. However, these models require long computation time and are difficult to be incorporated into some design optimization routines. Moreover, the computational burden can drastically increase for an ATEG with hundreds of ATECs. Thus, global structural optimization of ATEG using this modeling approach is rarely seen in the literature.

In view of the above, it is very challenging to optimize the performance of an ATEG system with the consideration of the micro-geometry of the ATECs. To solve the problem, we propose a fluid-thermal-electric multiphysical mathematical model with which the ATEG performance can be analyzed and optimized considering the micro-geometry of the ATECs and fluid channel structure. The primary contributions of this study are summarized as follows:

Table 1
Recent advances in modeling methods for ATECs and ATEGs.

Research subject	Model type	Modeling method/ Software	Features	References
ATEC	coupled thermal-electric mathematical model	finite element method/ Matlab	constant boundary condition one-dimensional steady state short calculation time	[16,22,26,37]
		Mathematical calculation	convective/ constant boundary conditions short calculation time one-dimensional steady state	[18,19,23]
		finite element analysis/ ANSYS	three-dimensional steady state relatively long calculation time	[31]
		finite element method/ COMSOL	constant boundary condition three-dimensional steady and transient state relatively long calculation time	[21,24,27–30]
A single ring of an ATEG	coupled thermal-electric mathematical model	finite element analysis/ ANSYS	constant boundary condition three-dimensional steady state relatively long calculation time	[20]
		finite element method/ Matlab	multiple boundary conditions one-dimensional steady state short calculation time	[38]
ATEG system	fluid-thermal-electric numerical model	thermal resistance network/ Matlab	multiple boundary conditions two-dimensional steady state short calculation time	[25,36,39]
		finite element method combined with thermal resistance	physical field distributions two-dimensional steady state	[15,34,35]

(continued on next page)

Table 1 (*continued*)

Research subject	Model type	Modeling method/ Software	Features	References
		network/ Matlab	short calculation time	
	CFD and thermal-electric numerical coupling model	finite element method/ COMSOL	multiple boundary conditions physical field distributions three-dimensional steady state long calculation time	[33,40]

1) A novel dual finite element method is developed to solve the proposed fluid-thermal-electric multiphysical model, establishing an accurate system-level mathematical model of automobile ATEG.
2) The effect of ATEC geometry on thermoelectric performance is analyzed from the perspective of the automotive ATEG system considering different vehicle speeds. Based on the analysis results, some new recommendations are made for future ATEG design.
3) Multi-objective global optimization was carried out to determine and compare the structural parameters of a single ATEC, a single ring of ATEG, and the entire ATEG. To our best knowledge, this is the first work that different levels of ATEG designs are carried out and compared with the same design criteria.

2. Modeling of ATEG

2.1. Physical model

Fig. 2(a) depicts an overall schematic of the proposed ATEG system. The system comprises an ATEG set, a cylindrical exhaust heat exchanger

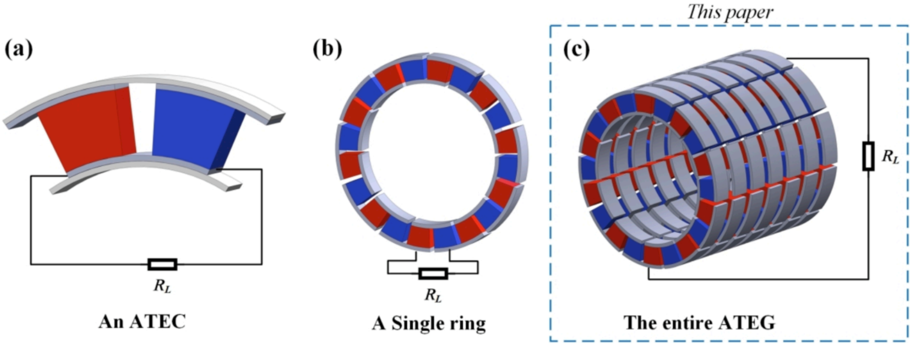

Fig. 1. Structural optimization objects of ATEGs: (a) individual ATEC, (b) a single ring of the ATEG, and (c) the whole ATEG.

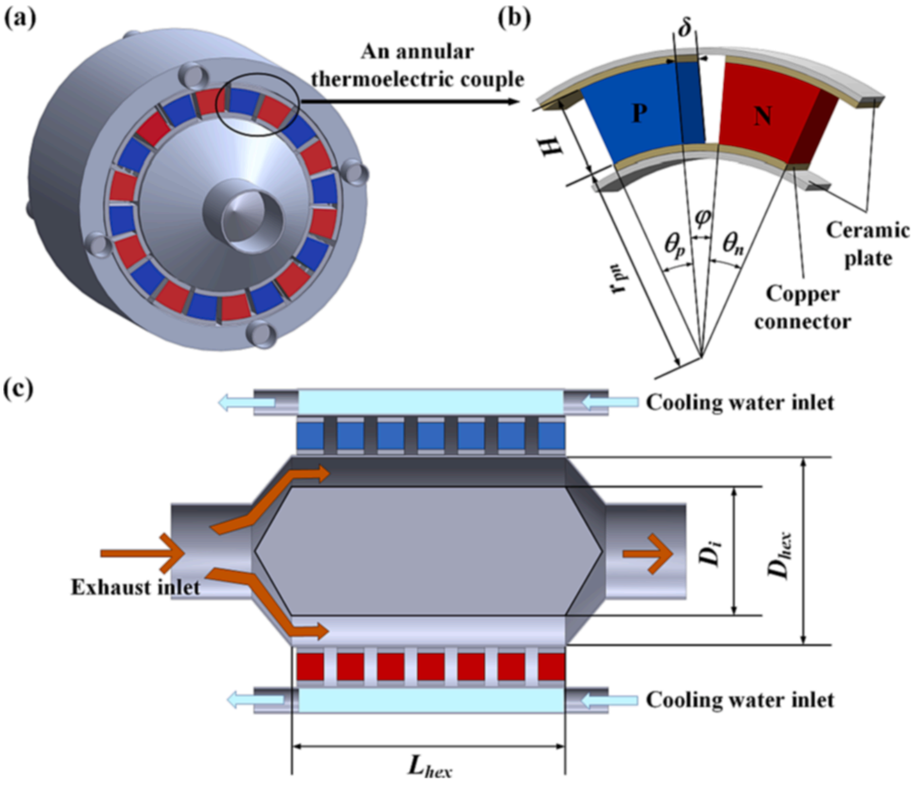

Fig. 2. Schematic diagram of the proposed ATEG: (a) overall structure, (b) 3D view of an annular thermoelectric couple, and (c) axial section view.

with an internal hollow cylinder (concentric annular heat exchanger), and an external cooling water jacket. When the heat source flows through the hot-end heat exchanger and the cooling water flows through the external cooling water jacket, the big temperature difference causes directional movement of the ions inside the thermoelectric semiconductors, resulting in a voltage difference.

Fig. 2(b) depicts a typical 3D structure of an ATEC. In each ring, q pairs of ATECs were uniformly distributed. Each ATEC comprises a p-type and an n-type thermoelectric semiconductor, a conductive copper sheet, and a ceramic plate on both sides. The distance between each ring is 1.5 mm. Here, H, δ, and θ denote the height, thickness, and angle of the semiconductor legs, respectively. The inner radius of the ATEC is denoted by r_{pn}. The angle of the gap between the legs is $\varphi = 1.5^\circ$. The subscripts "p" and "n" refer to the p-type and n-type semiconductors, respectively. The physical parameters of a commercial bismuth telluride thermoelectric material are all functions of temperature in this study.

A cross-section of the proposed ATEG is shown in Fig. 2(c). The exhaust flows into the device and is then directed to the annulus duct along the hollow cylinder inside the heat exchanger. This structure can increase the convective heat transfer efficiency and retain the high temperature at the hot end of the ATEC to maximize power generation. Here, D_i is the diameter of the hollow cylinder inside the heat exchanger, and L_{hex} and D_{hex} are the length and outer diameter of the heat exchanger, respectively. The cold end of the thermoelectric component is cooled by circulating water, with the heat source and cooling fluid flowing in the opposite direction. The shape factors in this study include heat exchanger dimensions (D_i and L_{hex}), and thermocouple dimensions (H, δ, and θ). The effects of these structural parameters on ATEG thermoelectric properties will be discussed in later sections.

2.2. Theoretical model

In previous studies, the finite element meshes were typically created by dividing the region either along the ATEC height direction [16,26,38] or along the fluid flow direction [34,35,42]. In contrast, we propose a dual finite element modeling/solution method to simulate the ATEG with improved accuracy in this work. In this method, we simultaneously create the finite element meshes by dividing the region in the thermal fluid flow direction (x-direction) and the ATEC height direction (r-direction). The ATECs inside ATEG can be grouped into n rings along the fluid flow direction, as shown in Fig. 3(a). The ring is further discretized into m computational units to calculate the key parameters separately, and each computational unit consists of a pair of ATECs. The schematics of the ith ($i = 1, 2, \cdots, m$) unit in the jth ring ($j = 1, 2, \cdots, n$) are shown in Fig. 3(b). When constructing this theoretical model, the following assumptions are made: 1) The surface thermal radiation is ignored, 2) all thermoelectric semiconductors are thermally insulated from each other, 3) the Thomson effect is ignored, and 4) the internal and external loads of the closed-loop circuit are matched.

2.2.1. Heat transfer in the fluid flow direction

In the ATEG, the hot and cold fluids flow into the system at temperatures T_{fin} and T_{win}, respectively. T_{fin} and T_{win} are equal to the temperatures of the corresponding first computational unit, i.e., $T_{fin} = T_f^1$, $T_{win} = T_w^{m+1}$, where T_f and T_w are the hot and cold fluid temperatures, respectively, as shown in Fig. 3(b). Furthermore, in Fig. 3(b), T_h and T_c denote the hot- and cold-end surface temperatures of the thermoelectric legs, respectively. For the hot fluids, the outlet temperature of the $(j-1)$th computational unit is considered as the inlet temperature of the jth computational unit, and vice versa for cold fluids.

The hot-end heat flow Q_h^j and cold-end heat flow Q_c^j of the ith ring can be obtained by considering the Peltier heat, Joule heat, and Fourier conductive effect, i.e.,

$$Q_h^j = q\left[\alpha_{pn}^j I^j T_h^j + K_{pn}^j \left(T_h^j - T_c^j\right) - 0.5\left(I^j\right)^2 R_{pn}^j\right] \tag{1}$$

$$Q_c^j = q\left[\alpha_{pn}^j I^j T_c^j + K_{pn}^j \left(T_h^j - T_c^j\right) + 0.5\left(I^j\right)^2 R_{pn}^j\right] \tag{2}$$

$$I^j = q\alpha_{pn}^j \left(T_h^j - T_c^j\right) \Big/ \left[R_L^j + q\left(R_{pn}^j + R_{cu}^j\right)\right] \tag{3}$$

Here, q is determined by the angles θ_p and θ_n of the p- and n-type thermoelectric legs as well as the angle φ of the gap in between (see Fig. 2(b)), i.e.,

$$q = 360^\circ \Big/ \left(2\varphi + \theta_p + \theta_n\right), \varphi = 1.5^\circ \tag{4}$$

and q will be rounded down if it is not an integer. The Seebeck coefficient α_{pn}, resistance R_{pn}, and thermal conductance K_{pn} are calculated as follows

$$\alpha_{pn}^j = \overline{\alpha_p^j} - \overline{\alpha_n^j} \tag{5}$$

$$R_{pn}^j = \frac{\overline{\rho_p^j}\ln\left[\left(r_{pn} + H_p\right)/r_{pn}\right]}{\delta_p\theta_p} + \frac{\overline{\rho_n^j}\ln\left[\left(r_{pn} + H_n\right)/r_{pn}\right]}{\delta_n\theta_n} \tag{6}$$

$$K_{pn}^j = \frac{\delta_p\theta_p\overline{\lambda_p^j}}{\ln\left[\left(r_{pn} + H_p\right)/r_{pn}\right]} + \frac{\delta_n\theta_n\overline{\lambda_n^j}}{\ln\left[\left(r_{pn} + H_n\right)/r_{pn}\right]} \tag{7}$$

where $r_{pn} = \delta_{wa} + \delta_{cu} + \delta_{cer} + D_{hex}/2$ denotes the inner radius of the p/n-type semiconductor leg. The overbars in the above equations represent the averaged parameters. They are calculated by

$$\overline{\alpha_p^j} = \left[\int_{T_c^j}^{T_h^j} \alpha_p(T)dT\right] \Big/ \left[T_h^j - T_c^j\right] \tag{8}$$

$$\overline{\alpha_n^j} = \left[\int_{T_c^j}^{T_h^j} \alpha_n(T)dT\right] \Big/ \left[T_h^j - T_c^j\right] \tag{9}$$

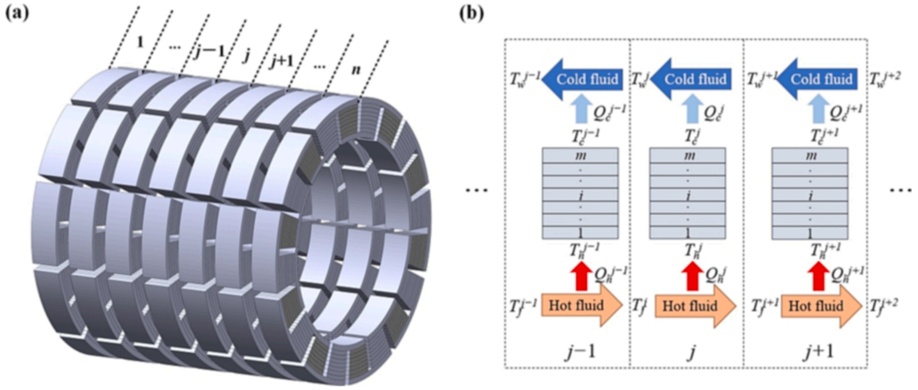

Fig. 3. Schematics of proposed finite element method: (a) Finite element meshing; (b) Heat transfer process and temperature relationships.

$$\overline{\rho_p^j} = \left[\int_{T_c^j}^{T_h^j} \rho_p(T)dT\right] \Big/ \left[T_h^j - T_c^j\right] \tag{10}$$

$$\overline{\rho_n^j} = \left[\int_{T_c^j}^{T_h^j} \rho_n(T)dT\right] \Big/ \left[T_h^j - T_c^j\right] \tag{11}$$

$$\overline{\lambda_p^j} = \left[\int_{T_c^j}^{T_h^j} \lambda_p(T)dT\right] \Big/ \left[T_h^j - T_c^j\right] \tag{12}$$

$$\overline{\lambda_n^j} = \left[\int_{T_c^j}^{T_h^j} \lambda_n(T)dT\right] \Big/ \left[T_h^j - T_c^j\right] \tag{13}$$

where α, ρ, and λ denote the Seebeck coefficient, resistivity, and thermal conductivity, respectively.

Furthermore, considering the convective heat transfer rate of the fluid, $Q_{trans,f}$ denotes the heat transported by the thermal fluid, and $Q_{trans,c}$ denotes the heat transported by the cold fluid, i.e.,

$$Q_{trans,f}^j = c_f^j m_f \left(T_f^j - T_f^{j+1}\right) \tag{14}$$

$$Q_{trans,c}^j = c_w m_w \left(T_w^j - T_w^{j+1}\right) \tag{15}$$

In addition, considering the irreversibility of the finite heat transmission, the heat flow $Q_{conv,f}$ of the jth ring can be expressed as

$$Q_{conv,f}^j = qA_h k_f^j \left[0.5\left(T_f^j + T_f^{j+1}\right) - T_h^j\right] \tag{16}$$

where k_f is determined by the convective heat transfer thermal resistance $R_{f,conv}$, the thermal resistance of the heat exchanger's outer wall $R_{f,wa}$, the thermal resistance of the copper sheet $R_{f,cu}$, and the thermal resistance across the ceramic sheet $R_{f,cer}$, i.e.,

$$\begin{aligned} k_f^j &= 1\Big/\left(R_{f,conv}^j + R_{f,wa}^j + R_{f,cu}^j + R_{f,cer}^j\right) \\ &= 1\Big/\left(1/h_f^j + \delta_{wa}/\lambda_{wa}^j + \delta_{cu}/\lambda_{cu}^j + \delta_{cer}/\lambda_{cer}^j\right) \end{aligned} \tag{17}$$

and h_f is the convective heat transfer coefficient obtained from the Gnielinski correlation [35,41]:

$$h_f^j = Nu^j \cdot \lambda_f^j \Big/ (D_{hex} - D_i) \tag{18}$$

$$Nu^j = \frac{Pr^j(F^j/8)(Re^j - 1000)\left[1 + \left(\frac{D_{hex}-D_i}{L_{hex}}\right)^{2/3}\right]}{1 + 12.7\sqrt{F^j/8}\left[(Pr^j)^{2/3} - 1\right]} \left[\frac{\left(T_f^j + T_f^{j+1}\right)\Big/2}{\left(T_{h,hex}^j + T_{h,hex}^{j+1}\right)\Big/2}\right]^{0.45} \tag{19}$$

$$F^j = \left(1.8\log Re^j - 1.5\right)^{-2} \tag{20}$$

where $T_{h,hex}$ represents the hot end heat exchanger's wall temperature. The heat exchanger length L_{hex} is determined by the thickness δ of thermoelectric legs, the gap δ_{gap} between each ring, and the number of rings n, i.e., $L_{hex} = n\ (\delta + \delta_{gap})$. The Reynolds number Re of the exhaust gas is determined by

$$Re^j = v_f \omega_f (D_{hex} - D_i)/\mu_f \tag{21}$$

$$v_f^j = \frac{m_f}{\omega_f^j \pi\left[(D_{hex}/2)^2 - (D_i/2)^2\right]} \tag{22}$$

Similarly to $Q_{conv,f}$, the heat flow $Q_{conv,c}$ can be calculated by

$$Q_{conv,c}^j = qA_c k_w^j \left[T_c^j - 0.5\left(T_w^{j+1} + T_w^j\right)\right] \tag{23}$$

with

$$\begin{aligned} k_w^j &= 1\Big/\left(R_{w,conv}^j + R_{w,wa}^j + R_{w,cu}^j + R_{w,cer}^j\right) \\ &= 1\Big/\left(1/h_w^j + \delta_{wa}/\lambda_{wa}^j + \delta_{cu}/\lambda_{cu}^j + \delta_{cer}/\lambda_{cer}^j\right) \end{aligned} \tag{24}$$

where the definitions and calculations of the parameters are similar to Eq. (17) but not elaborated here for brevity.

According to the characteristics of the connection point and the continuity of the finite element meshes, we have $Q_h = Q_{conv,f}$ and $Q_c = Q_{conv,c}$. Since the heat released by the thermal fluid in the jth ring equals the heat absorbed by the ATECs, we have $Q_h = Q_{trans,f}$. Similarly, we have $Q_c = Q_{trans,c}$ for the cold end.

2.2.2. Heat transfer along the height direction of the thermoelectric legs

Fig. 4 shows how the ATECs in the jth ring are discretized into m computational units along the height direction in a p-type semiconductor leg.

Denoting the temperatures on the ith computational unit of the p- and n-type thermoelectric legs by $T_p^j(i)$ and $T_n^j(i)$, respectively, the ATEG hot-end heat flow Q_h and cold-end heat flow Q_c can be expressed as

$$\begin{aligned} Q_h^j = q\{&\left[\alpha_p^j(1) - \alpha_n^j(1)\right]T_h^j I^j + K_p^j(1)\left[T_h^j - T_p^j(2)\right] \\ &+ K_n^j(1)\left[T_h^j - T_n^j(2)\right] - 0.5\left(I^j\right)^2\left[R_p^j(1) + R_n^j(1)\right]\} \end{aligned} \tag{25}$$

$$\begin{aligned} Q_c^j = q\{&\left[\alpha_p^j(m) - \alpha_n^j(m)\right]T_c^j I^j + K_p^j(m)\left[T_p^j(m) - T_c^j\right] \\ &+ K_n^j(m)\left[T_n^j(m) - T_c^j\right] - 0.5\left(I^j\right)^2\left[R_p^j(m) + R_n^j(m)\right]\} \end{aligned} \tag{26}$$

where the Seebeck coefficient α, resistance R, and thermal conductance K are obtained from the following equations

$$\alpha(i) = \frac{\int_{T(i+1)}^{T(i)} \alpha dT}{T(i) - T(i+1)} \tag{27}$$

$$\rho(i) = \rho|_{\frac{T(i)+T(i+1)}{2}} \tag{28}$$

$$\lambda(i) = \lambda|_{\frac{T(i)+T(i+1)}{2}} \tag{29}$$

$$R_p^j + R_n^j = \sum_{i=1}^{m} \frac{\ln[r(i+1)/r(i)]}{\delta\theta}\left[\rho_p(i) + \rho_n(i)\right] \tag{30}$$

$$K_p^j + K_n^j = \sum_{i=1}^{m} \frac{\delta\theta}{\ln[r(i+1)/r(i)]}\left[\lambda_p(i) + \lambda_n(i)\right] \tag{31}$$

Here, $r(i)$ denotes the radius of the ith computational unit in the r-direction of the ATEC, given by

$$r(i) = r_{pn} + i \times (H/m) \tag{32}$$

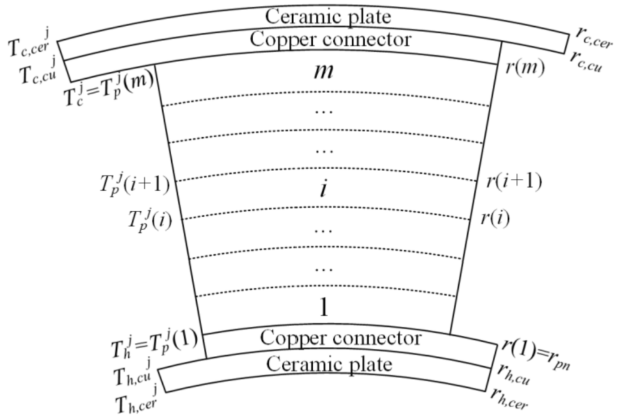

Fig. 4. Discretization of a single annular p-type semiconductor leg.

The heat released from the ith unit equals the heat absorbed by the (i + 1)th unit, i.e.,

$$\alpha_p^j(i)I^jT_p^j(i+1)+K_p^j(i)\left[T_p^j(i)-T_p^j(i+1)\right]+\frac{1}{2}\left(I^j\right)^2R_p^j(i)=$$
$$\alpha_p^j(i+1)I^jT_p^j(i+1)+K_p^j(i+1)\left[T_p^j(i+1)-T_p^j(i+2)\right]-\frac{1}{2}\left(I^j\right)^2R_p^j(i+1) \tag{33}$$

The hot-end temperature equals the temperature of the first computational unit, i.e., $T_h^j = T_p^j(1) = T_n^j(1)$ and $T_c^j = T_p^j(m) = T_n^j(m)$. The temperature of the (i + 1)th computational unit can be obtained. For example, for the p-type semiconductor, we have

$$T_p^j(i+1)=\frac{K_p^j(i)T_p^j(i)+K_p^j(i+1)T_p^j(i+1)+\frac{1}{2}\left(I^j\right)^2\left[R_p^j(i)+R_p^j(i+1)\right]}{K_p^j(i)+K_p^j(i+1)+\left[\alpha_p(i+1)-\alpha_p(i)\right]I^j} \tag{34}$$

The heat flow at both ends of the copper sheet, according to Eq. (25), can be expressed as

$$Q\left(r=r_{pn}\right)=Q_h^j=q\left[K_{cu}^j\left(T_{h,cu}^j-T_h^j\right)+0.5\left(I^j\right)^2R_{cu}\right] \tag{35}$$

$$Q\left(r=r_{h,cu}\right)=K_{cer}^j\left(T_{h,cer}^j-T_{h,cu}^j\right) \tag{36}$$

With Eqs. (25), (35), and (36), T_h can be obtained by

$$T_h^j=\frac{g_1T_{h,cer}^j+K_p^j(1)T_p^j(2)+K_n^j(1)T_n^j(2)+0.5\left(I^j\right)^2\left[R_p^j(1)+R_n^j(1)\right]+g_2\left(I^j\right)^2}{\left[\alpha_p^j(1)-\alpha_n^j(1)\right]I^j+K_p^j(1)+K_n^j(1)+g_1} \tag{37}$$

Similarly, T_c can be expressed as

$$T_c^j=\frac{g_3T_{c,cer}^j+K_p^j(m)T_p^j(m)+K_n^j(m)T_n^j(m)+\left\{0.5\left[R_p^j(m)+R_n^j(m)\right]+g_4\right\}\left(I^j\right)^2}{\left[\alpha_p^j(m)-\alpha_n^j(m)\right]I^j+K_p^j(m)+K_n^j(m)+g_3} \tag{38}$$

As shown in Fig. 4, $T_{h,cer}$ denotes the temperature of the contact surface between the ceramic and the heat source at the hot end, and $T_{h,cu}$ is the temperature of the contact surface between the copper connector and the ceramic plate at the hot end. The definitions of $T_{c,cu}$ and $T_{c,cer}$ are similar to $T_{h,cer}$ and $T_{h,cu}$, respectively. The expressions of coefficients g_1, g_2, g_3, and g_4 are provided in the Appendix.

2.2.3. Output performance evaluation

The voltage of the jth ring is the superposition of the open-circuit voltages of the m computational units, i.e.,

$$V_{oc}=q\sum_{i=1}^{m}\left\{\left[T_p^j(i)-T_p^j(i+1)\right]\alpha_p^j(i)-\left[T_n^j(i)-T_n^j(i+1)\right]\alpha_n^j(i)\right\} \tag{39}$$

The current I in the jth ring is calculated by

$$I^j=V_{oc}^j\Big/\left[R_L^j+q\left(R_p^j+R_n^j+R_{cu}^j\right)\right] \tag{40}$$

Then the total output power P_{out} and efficiency η of ATEG are expressed as

$$P_{out}=\sum_{j=1}^{n}\left(I^j\right)^2R_L^j \tag{41}$$

$$\eta=P_{net}\Big/\sum_{j=1}^{n}Q_h^j \tag{42}$$

The exhaust pressure drop increases with the introduction of the hollow cylinder, leading to higher convective heat transfer efficiency and a larger exhaust resistance. The net power P_{net} is introduced to evaluate the net power generation capacity of the ATEG:

$$P_{net}=P_{out}-P_{hex,loss} \tag{43}$$

$$P_{hex,loss}=\sum_{j=1}^{n}\frac{\Delta p^jm_f}{\rho_f^j}=\sum_{j=1}^{n}f_z^j\frac{Lm_f\left(v_f^j\right)^2}{2(D_{hex}-D_i)} \tag{44}$$

where ρ_f and Δp denote the density and pressure drop of the thermal fluid, respectively. The friction coefficient f_z of the thermal fluid is determined by [42]

$$f_z^j=\begin{cases}64\big/Re^j, & Re^j\leqslant 2000\\ \dfrac{0.3164}{\left(Re^j\right)^{0.25}}, & 2000<Re^j\leqslant\dfrac{59.7}{\left[2H_r/(D_{hex}-D_i)\right]^{8/7}}\end{cases} \tag{45}$$

2.3. Solution method

Fig. 5. shows the flow chart for solving this dual finite element numerical model, and the steps are described below. Given the ATEC and heat exchanger dimensions, the ATEG boundary conditions are first determined. The initial α_{pn}^j, K_{pn}^j, and R_{pn}^j are next calculated based on the fluid's average temperature that flows into the jth computational unit. By setting the initial heat transfer coefficient and current and with Eqs. (1)–(2), (14)–(16), and (23), the heat transfer rates Q_h^j and Q_c^j, fluid temperatures, and temperatures at both ends of the ATEC are solved using an iterative approximation method. Then, the temperatures of the thermocouple connection points, i.e., $T_p^j(1)$, $T_n^j(1)$, $T_p^j(m)$, and $T_n^j(m)$, are updated according to the temperatures at both ends of the ATEC. Next, the temperature distribution in the ATEC height direction is calculated using Eqs. (34), (37), and (38). If $Error_1$ is greater than a preset tolerance (10^{-6} is in this example), the updated temperature is used as the initial temperature and recalculated; otherwise, $\alpha_{pn,new}^j$, $K_{pn,new}^j$, and $R_{pn,new}^j$ are calculated based on the temperature distribution. If $Error_2$ exceeds the preset tolerance, the temperature distribution is recalculated with the updated parameters as the initial parameters until a converged solution is obtained. Finally, the output power, net power, and efficiency are solved according to Eqs. (39)–(45). The physical properties and parameters required for solving the model are shown in Table 2.

2.4. Boundary conditions

The ATEG under investigation is designed to recover exhaust waste thermal energy from suburban utility vehicles (SUVs), and the boundary conditions of ATEG are related to vehicle speed. The ATEG's inlet is connected to the three-way catalytic converter, and its outlet is connected to the muffler. It should be noted that because the cooling water tanks and the structure of ATEG differ significantly from those of the flat-type TEG, the external dimensions of ATEG should be much smaller than the distance between the chassis and the underside of the car. This can avoid any adverse effects on the normal operation of the vehicle.

In order to predict the performance of the ATEG set for real-world operation, we adopt the actual driving conditions of the SUV in the vehicle simulation package in ADVISOR [43]. The boundary conditions at the entrance of ATEG were measured and shown in Fig. 6. Here, the total vehicle weight is 1788 kg, the maximum engine power is 102 kW, the engine displacement is 3 L, and the car operates at a constant speed. The effect of vehicle speed on the inlet parameters of the ATEG cooling system channels was minimal. The mass flow rate m_w was maintained at 50 g/s, and the cooling water temperature fluctuated about 365.15 ± 2 K [44].

3. Model validation and performance analysis

3.1. Validation with mathematical models and experimental data

First, the automotive ATEG thermal resistance model developed by

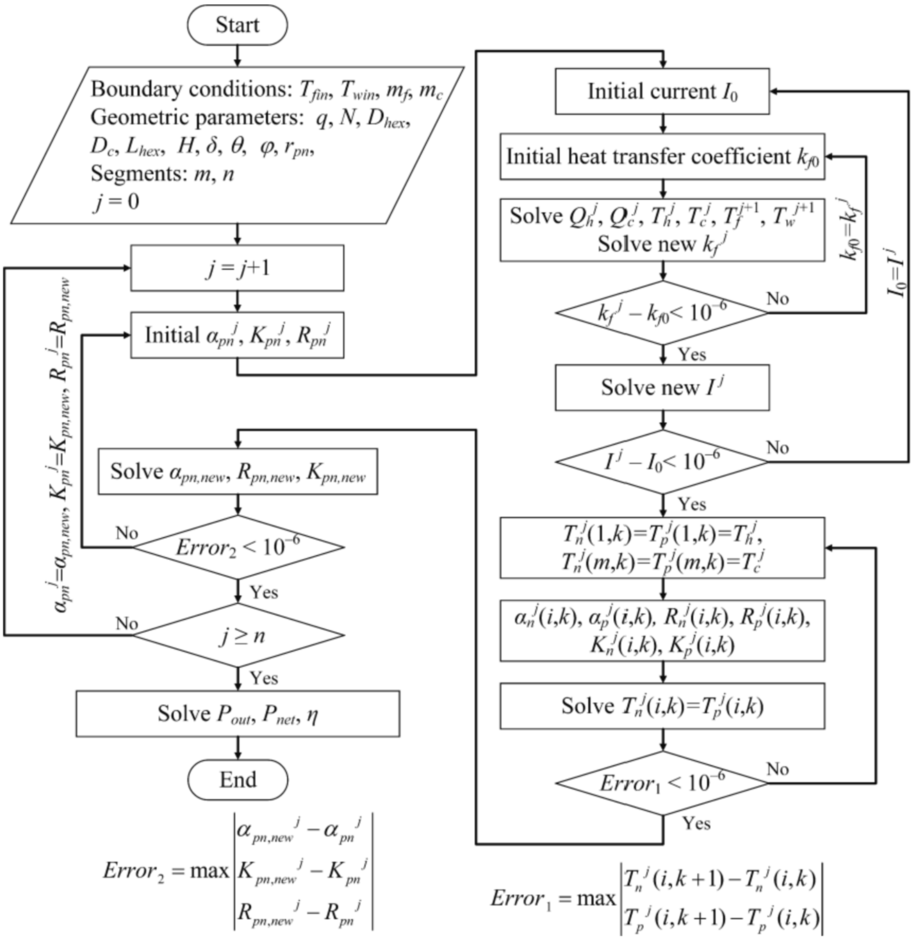

Fig. 5. Flow chart of the method to solve the proposed dual finite element numerical model.

Table 2
Detailed parameters and material properties.

Name	Material name	Material property	Value	Units
Ceramic plate	Alumina	Thermal conductivity	$\lambda_{cer} = 30$	W/(m·K)
		thickness	$\delta_{cer} = 0.002$	m
Copper connector	Copper	Thermal conductivity	$\lambda_{cu} = 400$	W/(m·K)
		thickness	$\delta_{cu} = 0.001$	m
Heat exchanger	Aluminum	Thermal conductivity	$\lambda_{wa} = 217.7$	W/(m·K)
		thickness	$\delta_{wa} = 0.0015$	m
		diameter	$D_{hex} = 0.1$	m
p-type Semiconductor	p-type Bi_2Te_3 [7]	Seebeck coefficient	$\alpha_p(T) = 1.134 \times 10^{-14}T^4 - 2.035 \times 10^{-11}T^3 + 1.11 \times 10^{-8}T^2 - 1.818 \times 10^{-6}T + 1.61 \times 10^{-4}$	V/K
		Thermal conductivity	$\lambda_p(T) = -1.242 \times 10^{-9}T^4 + 2.331 \times 10^{-6}T^3 - 1.575 \times 10^{-3}T^2 + 0.457\ T - 46.97$	W/(m·K)
		Electrical resistivity	$\rho_p(T) = -4.32 \times 10^{-16}T^4 + 8.94 \times 10^{-13}T^3 - 7.74 \times 10^{-10}T^2 + 3.519 \times 10^{-7}T - 5.01 \times 10^{-5}$	Ω·m
n-type Semiconductor	n-type Bi_2Te_3 [7]	Seebeck coefficient	$\alpha_n(T) = -1.3 \times 10^{-14}T^4 + 2.325 \times 10^{-11}T^3 - 1.42 \times 10^{-8}T^2 + 3.469 \times 10^{-6}T - 4.428 \times 10^{-4}$	V/K
		Thermal conductivity	$\lambda_n(T) = +1.537 \times 10^{-10}T^4 - 3.019 \times 10^{-7}T^3 + 2.246 \times 10^{-4}T^2 - 7.414 \times 10^{-2}T + 10.12$	W/(m·K)
		Electrical resistivity	$\rho_n(T) = 1.317 \times 10^{-16}T^4 - 2.305 \times 10^{-13}T^3 + 7.827 \times 10^{-11}T^2 + 4.507 \times 10^{-8}T - 8.072 \times 10^{-6}$	Ω·m
Hot fluid	Exhaust gas [41]	Specific heat capacity	$c_f(T) = 1.0731 - 5.7059 \times 10^{-4}T + 1.4411 \times 10^{-6}T^2 - 1.0838 \times 10^{-9}T^3 + 2.8163 \times 10^{-13}T^4$	J/(g·K)
		Dynamic viscosity	$\mu_f(T) = 2.68 + 6.098 \times 10^{-2}T - 2.8219 \times 10^{-5}T^2 + 7.005 \times 10^{-9}T^3$	10^{-6} Pa·s
		Density	$\omega_f(T) = 3.1589 \times 10^3 - 10.51\ T + 1.6237 \times 10^{-2}T^2 - 1.1708 \times 10^{-5}T^3 + 3.178 \times 10^{-9}T^4$	g/m^3
		Thermal conductivity	$\lambda_f(T) = -1.1 \times 10^{-3} + 1.046 \times 10^{-4}T - 5 \times 10^{-8}T^2 + 9 \times 10^{-12}T^3$	W/(m·K)
		Prandtl number	$Pr(T) = 0.7798 - 2 \times 10^{-4}T - 7 \times 10^{-7}T^2 + 2 \times 10^{-9}T^3 - 9 \times 10^{-13}T^4$	
Cold fluid	Water [42]	Specific heat capacity	$c_w = 4.177$	J/(g·K)
		convective heat transfer coefficient	$h_w = 1000$	W/(m^2·K)

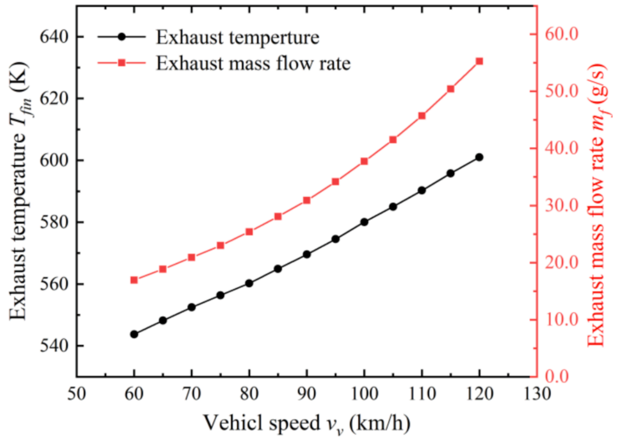

Fig. 6. Exhaust inlet parameters of ATEG under different vehicle speeds.

Shen et al. [39] was used to validate the present model. An ATEG system for automotive exhaust thermal energy recovery was established using a PbSnTe-based thermoelectric material where $H = 6$ mm, $\theta_p = \theta_n = 15^\circ$, and $\delta = 2$ mm. The boundary conditions are: $T_{fin} = 873$ K, $m_f = 46$ g/s, $T_{win} = 353$ K, and $m_w = 500$ g/s. The same parameters and thermoelectric material properties are used in the validation process. The simulation results are compared in Fig. 7(a). When L_{hex} less than 1 m, the error is less than 2 %; when $L_{hex} = 1.35$ m, the error reaches the maximum value of 3.9 %. The error occurs because the current model considers the temperature dependence of thermal fluid properties: The dynamic viscosity coefficient, Prandtl number, density, specific heat capacity, and thermal conductivity are not constant but functions of temperature. Furthermore, the ATEG length studied in this paper is generally less than 1 m due to the structure of the vehicle exhaust system. Therefore, the results of the proposed and the reference models match well.

Although a ring thermoelectric module has been proposed [45], its geometry and electrical connections differ from the conventional ATEGs [15–27]. Hence, the result in [45] is not suitable for model comparison and validation. Instead, experimental data from a conventional automotive TEG is used for model validation. Niu et al. [46] constructed an automobile TEG by combining a commercial Bi_2Te_3-based thermoelectric module with a heat exchanger for an experimental test. The heat exchanger is made of a 1-mm thick purple copper plate, and 56 thermoelectric modules are closely arranged between the cold fluid channels and the heat exchanger. Fig. 7(b) shows the variation of TEG output power with the load resistance at $T_{fin} = 393$ K. The average error between the model in this paper and the experimental data is 3.1 %. As a high-fidelity physics-based model, the proposed model shows higher accuracy than the model in [34]. The error between experimental data and simulation results of the proposed model is caused by the following: 1) The contact thermal resistance and contact resistance are ignored since the experiment does not provide them; 2) The experimental wire resistance and TEG heat loss are neglected; 3) Error exists between the measured value and the theoretical values. In fact, the present study mainly focuses on the condition of matching the internal and external loads so that these errors can be neglected. Therefore, the proposed model is considered to be able to predict the performance of the automotive ATEG accurately.

3.2. Model performance analysis

To demonstrate the characteristics and superiority of the proposed mathematical model, Fig. 8 depicts the detailed physical field distribution of the ATEG when $v_v = 60$ km/h. Six rings were constructed, each containing 12 ATECs. Fig. 8(a) depicts the temperature variations in the ATEC height direction as well as the fluid flow direction. The detailed Seebeck voltage and current distribution can also be obtained according to Eqs. (39) and (40). Fig. 8(b) shows the variations in fluid temperature, Reynolds number, flow rate, and heat transfer coefficient along the fluid flow direction. Therefore, the proposed model can be used to predict the detailed distribution of fluid-thermal-electric multiphysical fields in the automotive ATEG.

Fig. 7(b) compared the simulation results of the proposed model and a comprehensive numerical ATEG model developed in our previous work [34] with the experimental data. The maximum error between the simulation results in [34] and the experimental data is less than 8 %. The proposed model can thus obtain much more accurate results compared to the model in [34]: The accuracy of the mathematical model proposed in this study was improved by 62 %. As mentioned earlier, this improvement is achieved by discretizing each pair of thermocouples into m computational units along the height direction and introducing a triple iterative process to find the optimal approximate solution. It is worth noting that, even though the iterative process has increased the algorithmic complexity, the computational efficiency of the new model is not significantly reduced. The CPU execution time is less than 10 s. Compared to the proposed method, the ATEC finite element models built by COMSOL [47–49] and the neural network-trained simulation models [50] are much more time-consuming. In addition, although a multi-objective optimization algorithm is an effective tool for finding optimal solutions under multivariate and multiple conditions, some papers have performed structural optimization of FTEGs using some of the methods mentioned above [51,52], but at the expense of high computational cost. On the other hand, few studies have been conducted on ATEGs. The mathematical model proposed in this paper enables high-precision simulation from a single ATEC to the entire TEG.

4. Results and discussion

As shown in Fig. 9, when the structural parameters of the thermoelectric legs vary, the overall structure of the ATEG changes

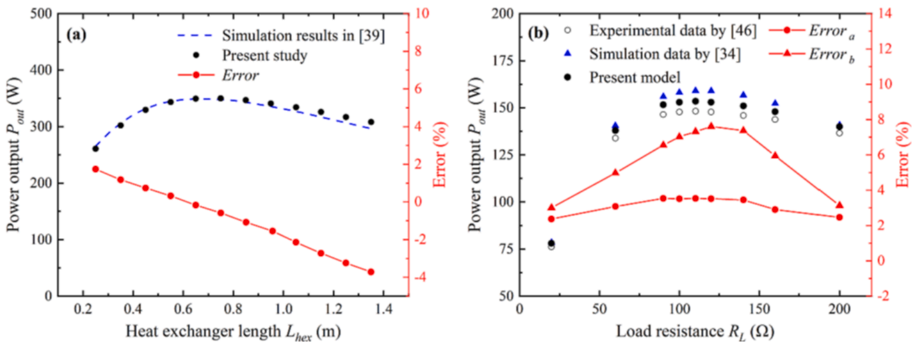

Fig. 7. Validation of the proposed analytical model: (a) Comparison with simulation results from Ref. [39]. (b) Comparison with experimental data from Ref. [46] and simulation results from Ref. [34]. (*Error*$_a$: error between the present model and experimental data; *Error*$_b$: error between Ref. [34] and experimental data).

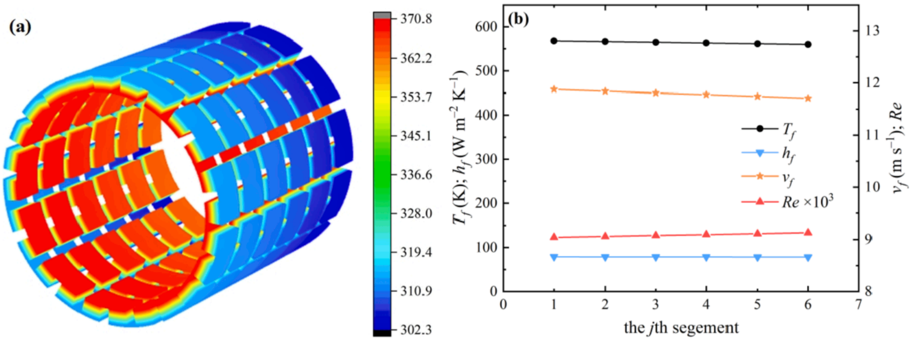

Fig. 8. Detailed distribution of the (a) ATEC temperature and (b) hot fluid parameters. ($H = 5$ mm, $\theta = 13.5°$, $\delta = 5$ mm).

considerably. Fig. 9(a) serves as a control group, where $H = 5$ mm, $\theta = 21°$, and $\delta = 5$ mm. Fig. 9(b), (c), and (d) show the schematics of the ATEG when $H = 10$ mm, $\theta = 9.75°$, and $\delta = 10$ mm, respectively. Therefore, the effect of ATEC structural parameters on the thermoelectric performance of ATEG should be analyzed under global considerations rather than optimizing the optimal parameters of individual ATECs. This is one of the main contributions that differ the present work from existing studies, and the results will be analyzed in detail in this section.

The outer diameter D_{hex} of the heat exchanger is generally fixed by the size of the vehicle exhaust system, as described in Section 2.4, and in this study, we set $D_{hex} = 0.1$ m. Therefore, the effect of the inserted hollow cylinder diameter D_i on the ATEG is mainly studied. Define the dimensionless diameter.

$$\gamma = D_i / D_{hex} \tag{46}$$

where γ denotes the inner to outer diameter ratio of the heat exchanger with a concentric annular channel.

Since the cross-section of the ATEC is not in a rectangular form, all the structural parameters investigated in this paper will affect the volume of the ATECs (denoted by V_{ATEC}). To evaluate the net power generated per unit volume, we define the net power volume density PD_V, as the ratio of the net power to the volume of all ATECs:

$$PD_V = P_{net} / V_{ATEC} \tag{47}$$

Compared to the net power P_{net}, PD_V is considered a more suitable indicator for evaluating the output performance of ATEG, particularly in automotive applications where a high power output with the smallest possible volume is required.

4.1. Effect of thermoelectric leg height, H

The effect of thermoelectric leg height H on the thermoelectric performance at different vehicle speeds is shown in Fig. 10 for $\theta = 4.5°$ and $\delta = 2$ mm. As shown in Fig. 10(a) and (b), the net power and efficiency increase with leg height, but the growth rate reduces gradually. This is

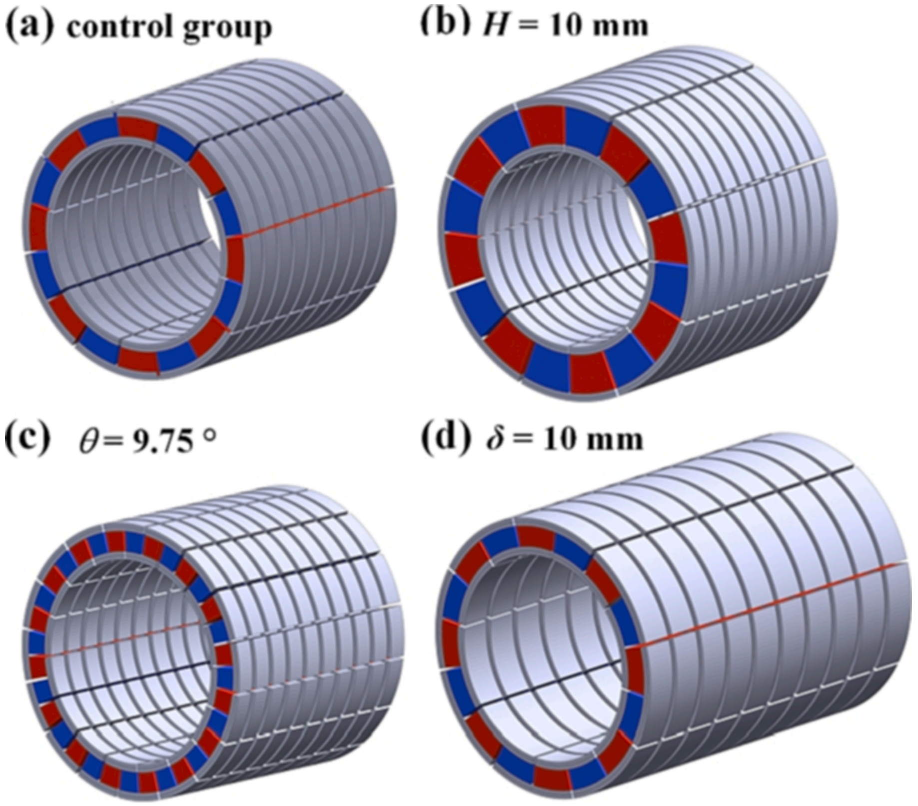

Fig. 9. Schematic diagram of the ATEG with different ATEC structural parameters: (a) control group, $H = 5$ mm, $\theta = 21°$, $\delta = 5$ mm. (b) $H = 10$ mm; (c) $\theta = 9.75°$; (d) $\delta = 10$ mm.

because the thermal resistance of the thermoelectric leg gradually increases as H becomes larger, increasing the temperature difference between the two ends and improving the thermoelectric performance. However, the additional electric potential obtained is gradually consumed by the internal resistance of the thermoelectric legs as H increases. Furthermore, when the vehicle speed exceeds 100 km/h, the net power increases first and gradually decreases. The reason is that there is a limit on the convective heat transfer effect between the hot end of the thermoelectric module and the hot fluid. Therefore, continuously increasing the heat flow density will cause a slow increase in the power of the ATEG [53], while the high mass flow rate of exhaust gas will result in a loss of engine pumping power [42]. As a result, it is unsuitable to choose higher thermoelectric legs for all ATECs because such a design cannot effectively increase the net power when the entire automobile ATEG is considered.

Interestingly, the single-loop ATEC model developed by Zhu et al. [38] showed that as leg height increases, the efficiency could increase, but the output power decreases. The contradictory conclusion is due to that in applications where the temperature difference is small, increasing the leg height can result in excessive electric potential consumption due to the internal resistance of the ATEC. In fact, the output power of the automotive ATEG increases with a larger H, which corroborates the results of Shen et al. [39]. It also illustrates that when many ATECs are coupled together to form an ATEG for practical applications, the thermoelectric performance might differ from that of a single thermoelectric couple.

As shown in Fig. 10(c), the power density PD_V decreases as H increases. Higher ATECs require more thermoelectric materials, leading to larger weights and sizes. It should also be noted that slender thermoelectric legs should be avoided during design because it reduces ATEG stability and service life, particularly in the automotive exhaust recovery system.

In general, the higher the vehicle's speed and lead to the higher values of mass flow rate, vehicle exhaust temperature, and the amount of heat. As a result, the operating temperature difference amongst the ATECs increase with vehicle speed, as shown in Fig. 10(d). However, according to the material properties of thermoelectric semiconductors, the thermal conductivity and resistivity increase with rising temperature (Table 2), leading to a degradation in performance. Therefore, increasing the vehicle speed will cause lowered net power, efficiency, and power density. For example, when $H = 6$ mm, the calculated average net power, average power density, and average temperature difference are 74.39 W, 261.7 W/m^3, and 106.3 K, respectively. When H is doubled, although there is an increase of 42.5 % in the average temperature difference, the resulting average net power can only increase by 10 %, and the average power density decreases by 47.9 %.

4.2. *Effect of thermoelectric leg angle, θ*

This section will examine the effect of the thermoelectric leg angle θ on the ATEG output performance. When the gap between the ATECs in each ring remains constant, a change in θ affects the number of thermoelectric legs within a ring as well as the heat transfer area, as described in Eq. (4). On the other hand, the number of ATECs and the heat transfer area significantly influence the ATEG performance. As an example, the thermoelectric leg angle is selected as 2.25°, 3°, 4.125°, 6°, 9.75°, and 21° for investigation. The corresponding numbers of ATECs in a single ring are 48, 40, 32, 24, 16, and 8, respectively.

The effects of θ on net power P_{net}, efficiency η, and power density PD_V at different vehicle speeds are shown in Fig. 11(a), (b), and (c), respectively. It can be seen that larger thermoelectric leg angles improve the efficiency and power density, but the changing trend of the net power is in the opposite direction. This is because as the angle increases, the average operating temperature difference of the thermocouple in the direction of fluid flow decreases, resulting in lower output power. Meanwhile, as the thermal resistance of the ATECs decreases, the heat

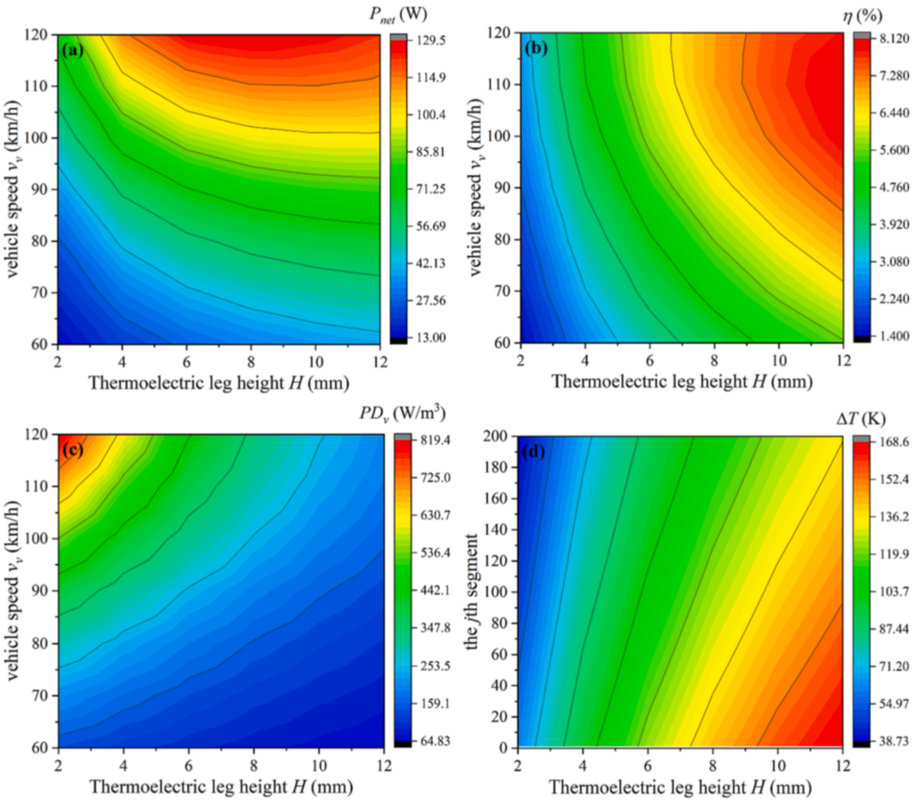

Fig. 10. Variations of (a) P_{net}, (b) η, and (c) PD_V with H under different v_v, and variations of (d) ΔT along the hot fluid flow direction under different H at $v_v = 120$ km/h. ($\theta = 4.5°$, $\delta = 2$ mm, and $\gamma = 0.8$).

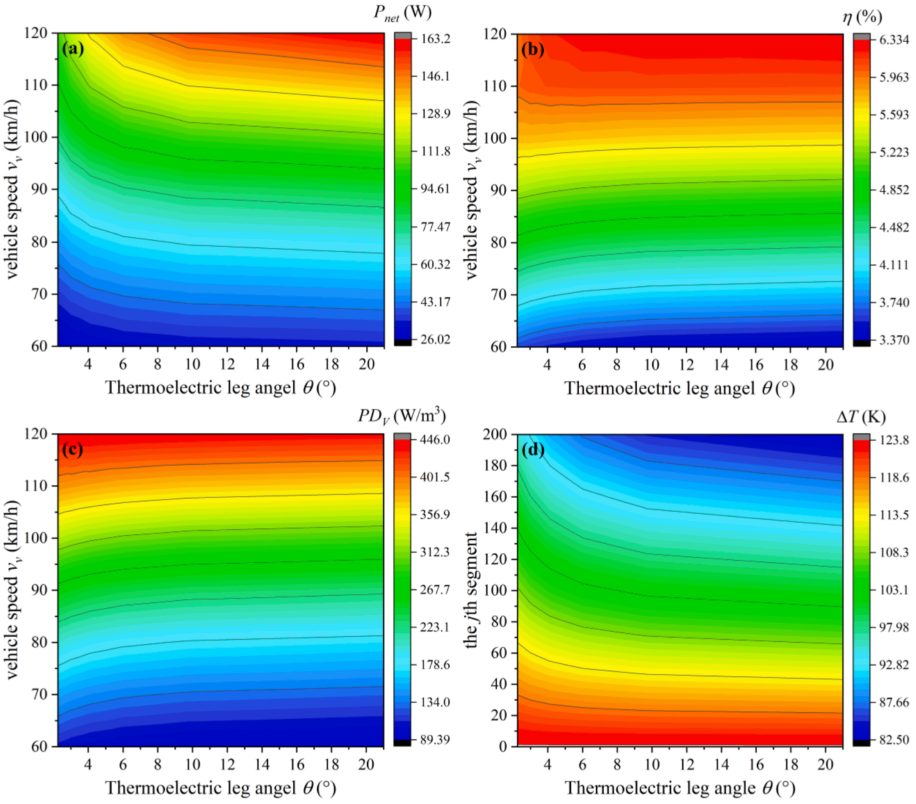

Fig. 11. Variations of (a) P_{net}, (b) η, and (c) PD_V with θ under different v_v, and variations of (d) ΔT along the hot fluid flow direction under different θ at $v_v = 120$ km/h. ($H = 6$ mm, $\delta = 2$ mm, and $\gamma = 0.8$).

transfer through the ATECs will increase, and the fluid temperature will decrease more, as shown in Fig. 11(d). In addition, the effect of vehicle speed on these trends was not significant. When $\theta > 9.75°$, the growth of η and PD_V slows down and P_{net} continues to fall. The temperature gradients of the thermal fluid becomes more obvious, leading to reduced thermoelectric performance of the equipment.

4.3. Effect of thermoelectric leg thickness, δ

The thickness δ_p/δ_n affects not only the geometry of an ATEC but also the total length L_{hex} of the TEG set. L_{hex}, on the other hand, will directly affect the back pressure of the vehicle exhaust duct, resulting in parasitic power losses, which will be discussed in detail in this section.

The variation of output power P_{out} and net power P_{net} with thickness δ at different vehicle speeds v_v are shown in Fig. 12(a). With increased δ, P_{out} first increases rapidly and then the increase rate drops gradually. This trend is in agreement with the results obtained by Zhu et al. [38]. According to Eq. (6), increasing the leg thickness can reduce the internal resistance of the ATEC, but it does not influence the output voltage. As a result, one can increase the current and output power P_{out} by simply increasing δ. Furthermore, as the δ increases, it is interesting to observe that the net power increases first before it drops at some peak point. This is because, for a specific number of rings, the thickness has a linear relationship with the total length of the ATEG. According to Eq. (44), increasing the length of the ATEG will increase the exhaust back pressure and exhaust resistance inside the heat exchanger, leading to an additional power loss P_{loss} in the engine. As v_v increases, P_{loss} becomes more significant. The variation of the pressure drop Δp with thickness δ at different vehicle speeds v_v is shown in Fig. 13. The optimum thickness corresponding to the peak net power is 5 mm at most vehicle speeds. When $v_v = 120$ km/h, the maximum net power can reach 260 W. In addition, Fig. 12(b) shows the variation of PD_V and η with δ for different v_v. It can be seen that PD_V follows the same trend as P_{out}, whereas as the thickness increases, the efficiency decreases. This is because an increase

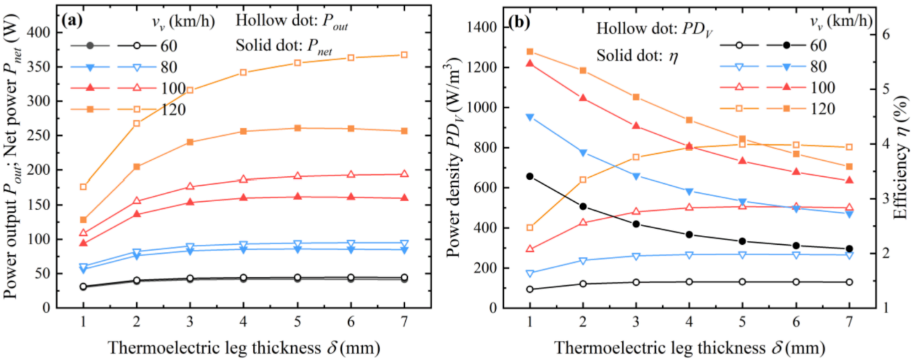

Fig. 12. Variations of (a) P_{out} and P_{net}, (b) PD_V and η with δ under different v_v at $H = 6$ mm, $\theta = 6°$, and $\gamma = 0.8$.

in the heat transfer area of ATECs and a decrease in thermal resistance can result in a smaller operating temperature difference and more heat transferred to the cooling system.

4.4. Effect of heat exchanger inner diameter, D_i

When the mass flow rate and the temperature in the engine exhaust are low, the exhaust cannot adequately fill the heat exchanger channel, resulting in low heat transmission efficiency. In this condition, the heat transfer capability of the ATEG can be improved by reducing the cross-sectional area of the internal exhaust channels, but this may also increase pressure drop. Therefore, the effect of the inner diameter D_i of the heat exchanger will be discussed in this section.

The effect of the dimensionless diameter γ on the exhaust pressure drop Δp at various vehicle speeds is illustrated in Fig. 14. As γ increases, the value of Δp increases slowly in the low-to-medium γ regions, while it grows drastically in the high γ region. This relationship can be explained as follows. According to Eq. (22), the exhaust gas flow rate is inversely proportional to the cross-sectional area of the heat exchanger. Since a larger γ will reduce the cross-sectional area, and according to Eq. (44), Δp is proportional to the exhaust gas flow rate, Δp will increase with γ.

Despite the increased back pressure, the output performance can still be improved. The effect of γ on P_{out} and P_{net} at different v_v is illustrated in Fig. 15(a). The hot end of the thermocouple absorbs more heat from the thermal fluid as γ increases, resulting in a larger operating temperature difference. Therefore, a larger γ can lead to higher output power. The trend of variation in net power, on the other hand, is different. When the vehicle moves slowly, the output power curve nearly coincides with the net power curve. As the vehicle speed increases, P_{net} increases first and then decreases with the increase of γ. When the vehicle speed is 120 km/h and $\gamma = 0.9$, the net power goes negative, indicating that high exhaust resistance will have a negative effect on the engine performance. When evaluating ATEG system performance, the different trends in P_{out} and P_{net} demonstrate the inadequacy of using a single output power as a metric for assessing the validity of optimization results. The dimensionless diameter γ should be less than 0.9 to maintain a suitable pressure drop in the exhaust system and avoid excessive power loss.

The variations of efficiency η and net power density PD_V with dimensionless diameter γ are shown in Fig. 15(b) and (c), respectively. Their trends are similar to the net power, indicating that the heat loss of ATEGs can be reduced by increasing the heat transmission efficiency of the hot-side heat exchanger so that the conversion efficiency can be effectively improved. In addition, increasing the vehicle speed can also effectively increase PD_V and η. For instance, when $v_v = 120$ km/h and $\gamma = 0.8$, the maximum net power and net power density are 236 W and 740 W/m^3, respectively, and the corresponding conversion efficiency is 5.33 %. Although the power density decreases when γ increases from 0.8 to 0.85, this is acceptable since the vehicle speed v_v is considered below 120 km/h most of the time.

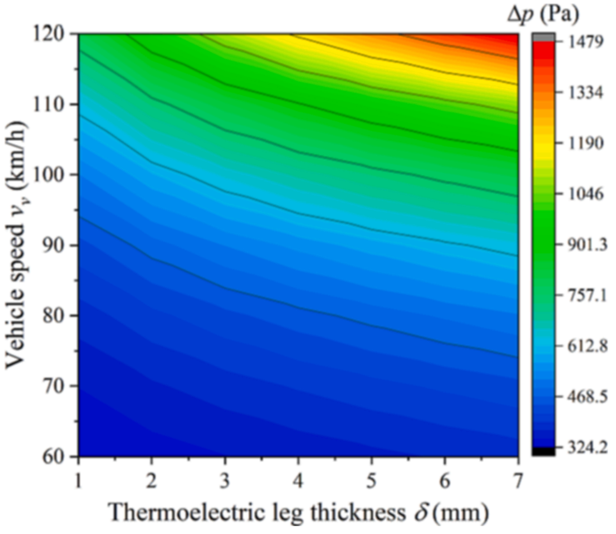

Fig. 13. Variations of Δp with δ under different v_v at $H = 6$ mm, $\theta = 6°$, and $\gamma = 0.8$.

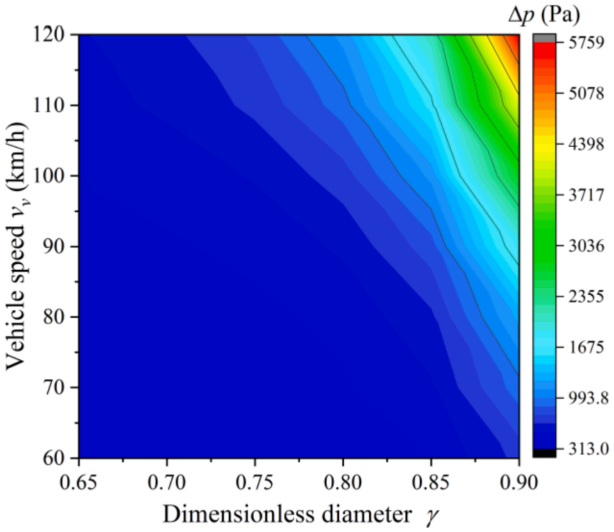

Fig. 14. Variations of Δp with γ under different v_v at $H = 6$ mm, $\theta = 6°$, and $\delta = 5$ mm.

4.5. Structural optimization with NSGA-II

From Section 4.1 to Section 4.4, we have seen that different ATEG structural parameters affect the thermoelectric properties differently. Compared with the optimization results from existing studies [27,54,55], the trend of the optimal ATEC size varies since the optimization objects are different. Furthermore, it is impossible to achieve optimal power, efficiency, and power density simultaneously by changing the structural parameters of the ATEG. This section will present the method to address this multi-objective optimization problem by considering a single ATEC, a single ring of ATEG, and the entire ATEG. The second-generation non-dominated sorting genetic algorithm (NSGA-II) [52] is used in this study to optimize the three competing objective functions of power, efficiency, and power density. The parameters of the algorithm used are set as follows. The population size is 300, the mutation probability is 0.3, the crossover probability is 0.9, the binary crossover parameter is 10, the polynomial variation parameter is 20, and the number of iterations is 1000. The flow chart of the algorithm is shown in Fig. 16. The decision variables are given in Table 3, where the corresponding searching ranges are also given, determined by actual operating conditions.

4.5.1. Multi-objective optimization with a single ATEC

When optimizing with a single ATEC, a p-type semiconductor and an n-type semiconductor are assumed to be connected by a copper sheet, and then a load is connected in series, as shown in Fig. 1(a). The decision variables are height H, angle θ, and thickness δ. Fig. 17 shows the set of Pareto solutions when $v_v = 120$ km/h. The point corresponding to the optimal design, determined using the Technique for Order of Preference by Similarity to Ideal Solution (TOPSIS), is indicated with arrows in the figure. The optimal output power, efficiency, and power density of the ATEC are 2.55 W, 5.2 %, and 11267 W/m^3, respectively. The optimal decision variables and output performance under different boundary conditions are listed in Table 4. It shows that the optimal height decreases slowly as the vehicle speed increases, but the angle and thickness remain at corresponding maximum values. As the vehicle speed

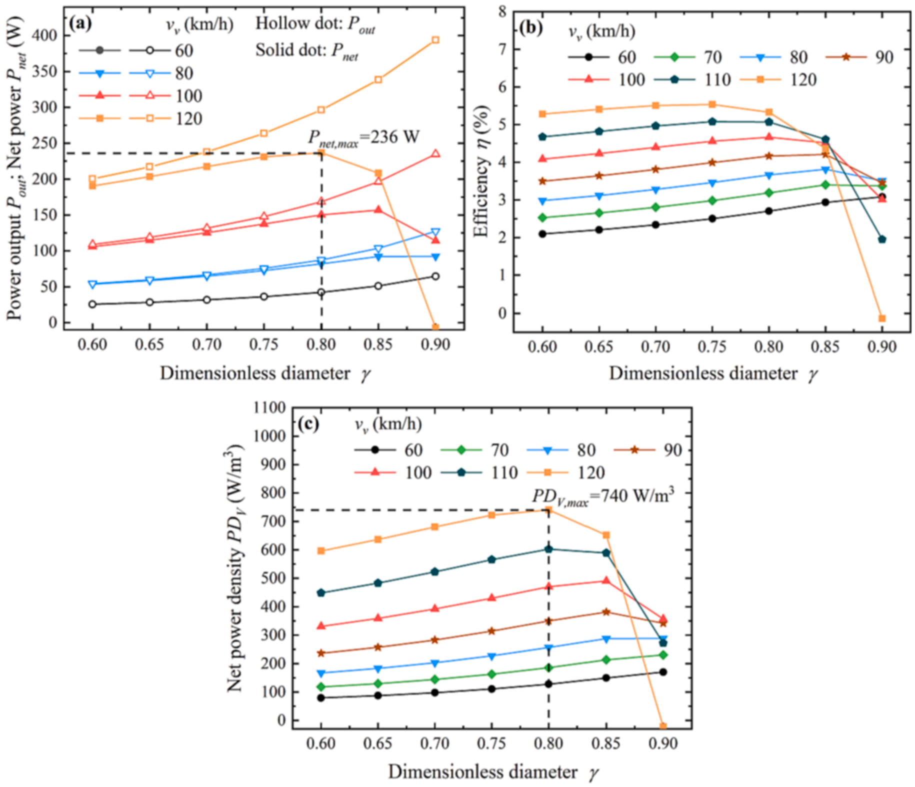

Fig. 15. Variations of (a) P_{out} and P_{net}, (b) η and (c) PD_V with γ under different v_v at $H = 6$ mm, $\theta = 6°$, and $\delta = 5$ mm.

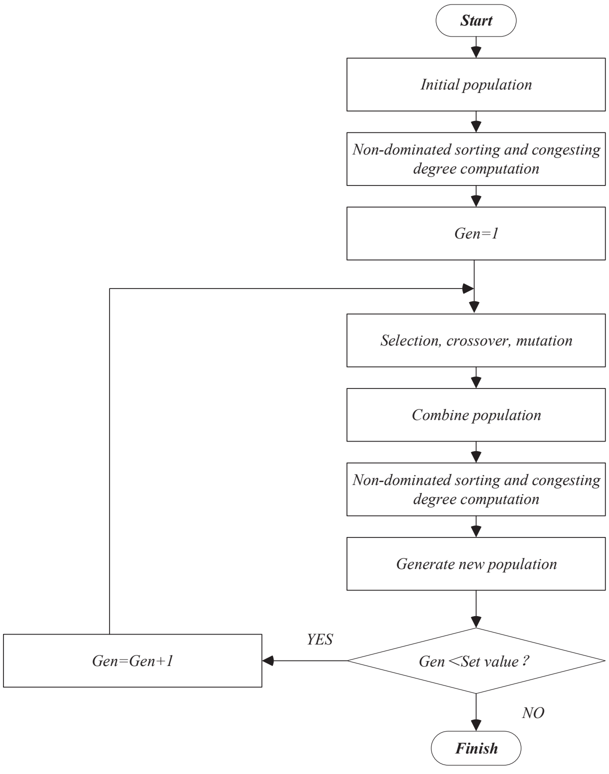

Fig. 16. Flow chart of NSGA-II.

increases, all three objective functions of the ATEC increase. This is because increasing the heat source temperature and mass flow rate can lead to a higher heat transfer coefficient and increased energy absorbed at the hot end, resulting in improved thermoelectric performance.

Table 3
Constraints on decision variables.

	H (mm)	θ (°)	δ (mm)	γ
Max	12	43.5	10	0.95
Min	2	2.25	2	0.6

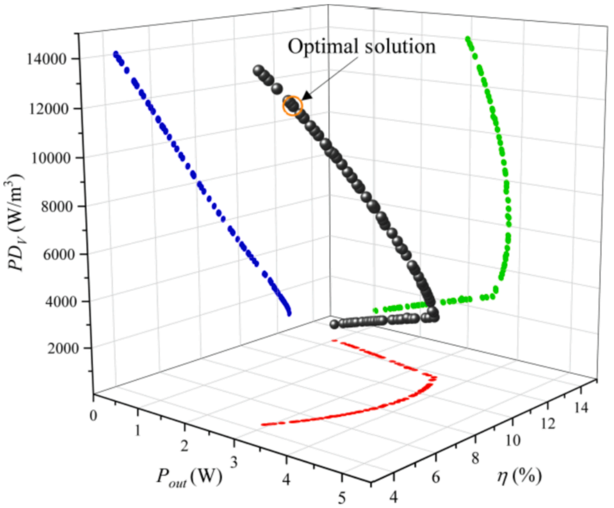

Fig. 17. Pareto set of optimal solutions with a single ATEC as the optimization object. ($v_v = 120$ km/h).

4.5.2. Multi-objective optimization with single ring ATEG

When optimizing with the single ring of ATEG, it is assumed that q pairs of ATECs are connected in series by copper sheets, and then a load is connected in series, as shown in Fig. 1(b). The decision variables are the same as that in the previous case, i.e., height H, angle θ, and

Table 4
The optimal values of structural parameters and optimum thermoelectric output performance with a single ATEC as the optimization object.

v_v (km/h)	H_{opt} (mm)	θ_{opt} (°)	δ_{opt} (mm)	P_{out} (W)	η (%)	PD_V (W/m^3)
60	3.6	43.5	10	0.82	4.35	2832.1
70	2.96	43.5	10	1.02	4.33	4229.5
80	2.65	43.5	10	1.26	4.44	5749.4
90	2.63	43.5	10	1.63	4.88	7295.6
100	2.43	43.5	10	2.03	4.98	9461
110	2.41	43.5	10	2.55	5.2	11,267
120	2.42	43.5	10	3.17	5.28	12760.3

thickness δ. Fig. 18 shows the set of Pareto solutions when $v_v = 120$ km/h, where the optimal output power, efficiency, and power density are 11.98 W, 6.04 %, and 16500 W/m^3, respectively. The optimal decision variables and output performance under different boundary conditions are listed in Table 5. It can be seen that the optimized parameters and trends of the decision variables are similar to the results of a single ATEC in the previous subsection.

4.5.3. *Multi-objective optimization with ATEG*

When optimizing with the entire ATEG, it is assumed that q pairs of ATECs are connected in series by copper sheets to form a single ring, as shown in Fig. 1 (c). The objective functions consider the net power, efficiency, and power density. Besides the height H, angle θ, and thickness δ, the decision variables also include the dimensionless diameter γ. Fig. 19 shows the set of Pareto solutions when $v_v = 120$ km/h, where the optimal output power, efficiency, and power density of the ATEG are 321.6 W, 6.58 %, and 634.15 W/m^3, respectively. The optimal decision variables and output performance under different boundary conditions are listed in Table 6. It can be seen that the optimized design parameters and their changing trends differ from that of the previous cases in Fig. 17 and Fig. 18. The optimized height and angle of the ATECs under the varying vehicle speed conditions are 12 mm and 2.25°, respectively. This is because when applied to the entire ATEG, there is a large temperature drop along the fluid flow direction, requiring a long thermoelectric leg for increased thermal resistance so that the temperature difference between the two ends of the ATEC can be maintained for better thermoelectric performance. Furthermore, the optimal thickness of the thermoelectric legs increases with vehicle speed, whereas the optimal dimensionless diameter γ of the heat exchanger decreases with increased vehicle speed.

Table 7 compares the performance of the three optimization results. Specifically, the structural parameters of all ATECs are set to the optimized values, and the ATEG's output performance is calculated separately. This ATEG has 200 rings and a dimensionless diameter of 0.74. The boundary condition is $v_v = 120$ km/h. It can be seen from Table 7 that, if the structural configuration parameters are optimized by considering the entire ATEG, the obtained net powers can be increased by 168 % and 197 %, respectively, compared to the results based on a single ATEC and a single ring. Furthermore, the power density is only reduced by about 20 %. Hence, when optimizing the structural

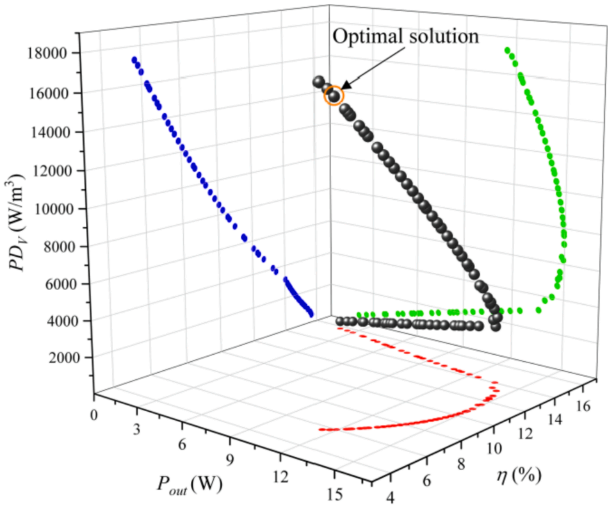

Fig. 18. Pareto set of optimal solutions with a single ring as the optimization object. ($v_v = 120$ km/h).

Table 5
Optimal values of structural parameters and optimum thermoelectric output performance with a single ring as the optimization object.

v_v (km/h)	H_{opt} (mm)	θ_{opt} (°)	δ_{opt} (mm)	P_{out} (W)	η (%)	PD_V (W/m^3)
60	3.9	43.5	10	3.35	4.66	2619.3
70	3.7	43.5	10	4.38	5.17	3755.5
80	3.3	43.5	10	5.33	5.33	5185.5
90	2.5	43.5	10	6.21	4.93	7705.9
100	2.32	43.5	10	7.82	5.28	10,477
110	2.2	43.5	10	9.62	5.58	13,462
120	2.19	43.5	10	11.98	6.04	16,500

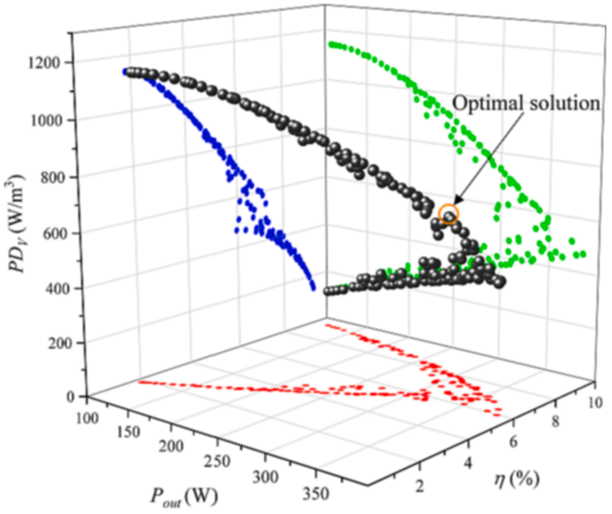

Fig. 19. Pareto set of optimal solutions with an ATEG as the optimization object. ($v_v = 120$ km/h).

Table 6
Optimal values of structural parameters and optimum thermoelectric output performance with an ATEG as the optimization object.

v_v (km/h)	H_{opt} (mm)	θ_{opt} (°)	δ_{opt} (mm)	γ_{opt}	P_{net} (W)	η (%)	PD_V (W/m^3)
60	12	2.25	4	0.906	65.68	4.8	132.36
70	12	2.25	5	0.889	88.91	5.02	178.53
80	12	2.25	6	0.864	115.3	5.2	232.43
90	12	2.25	6.7	0.085	149.47	5.58	301.18
100	12	2.25	7.9	0.819	196	5.88	395.0
110	12	2.25	10	0.79	260.6	5.93	514.26
120	12	2.35	10	0.74	321.6	6.58	634.15

Table 7
Performance comparison of the three optimization results.

	H_{opt} (mm)	θ_{opt} (°)	δ_{opt} (mm)	P_{net} (W)	η (%)	PD_V (W/m^3)
An ATEC	2.42	43.5	10	119.98	1.67	797.0
Single ring	2.19	43.5	10	108.28	1.5	796.6
ATEG	12	2.35	10	321.6	6.58	634.15

parameters of an ATEG, it is recommended to perform a global optimization with the entire ATEG as the optimization objective.

5. Conclusion

In this paper, a dual finite element method is proposed to construct and solve a fluid-thermal-electric multiphysical theoretical model of automotive ATEG. From the perspective of an ATEG system, the effects of four structural parameters on thermoelectric performance at various vehicle speeds were investigated. The multi-objective optimization problems are solved and compared for a single ATEC, a single ring of ATEG, and the entire ATEG. Based on the results, the main findings are concluded as follows.

1) The proposed theoretical model can be used to simultaneously predict the thermal, electric, and fluid fields of the ATEG. The average error between the simulation results and the experimental data is 3.1 %, with a single calculation taking less than 10 s. This model is useful for rapid evaluation of the performance of the automotive ATEG system.
2) It is found that thicker thermoelectric legs can increase both output power and power density but will also result in a linear increase in the overall length of the ATEG unit. This can cause excessive exhaust back pressure, reducing net power and conversion efficiency while increasing power generation costs.
3) Most of the time, the dimensionless diameter γ positively correlates to output power. However, at high vehicle speeds, the net power, efficiency, and power density of increase and then decrease as γ increases.
4) The obtained optimal structural parameters of the ATEG are $H_{opt} =$ 12 mm, $\theta_{opt} = 2.35^{\circ}$, $\delta_{opt} = 10$ mm, and $\gamma_{opt} = 0.74$. Compared to the conventional methods based on a single ATEC and a single ring, the new results show an increase of 168 % and 197 % in the net power. However, the power density is reduced by about 20 % as an expense.

In addition to optimizing the leg geometry to improve the performance of the ATEG, it is also necessary to maintain a low exhaust pressure drop and enhance the heat transfer performance to increase the system's net power. This factor will be considered in our future work to design an improved ATEG heat transfer scheme.

Declaration of Competing Interest

The authors declare that they have no known competing financial interests or personal relationships that could have appeared to influence the work reported in this paper.

Data availability

Data will be made available on request.

Acknowledgments

This research was supported by the National Natural Science Foundation of China (51977164).

Appendix

The temperature of the $(i+1)$th computational unit of the n-type semiconductor is expressed as

$$T_n^j(i+1) = \frac{K_n^j(i)T_n^j(i) + K_n^j(i+1)T_n^j(i+1) + \frac{1}{2}\left(I^j\right)^2\left[R_n^j(i) + R_n^j(i+1)\right]}{K_n^j(i) + K_n^j(i+1) + \left[\alpha_n(i+1) - \alpha_n(i)\right]I^j} \tag{A.1}$$

The thermal conductance $K_{h,cer}^j$ of the hot end ceramic plate is

$$K_{h,cer}^j = \frac{4\pi\delta_{cer}\lambda_{cer}^j}{\ln r_{h,cu} - \ln r_{h,cer}} \tag{A.2}$$

The thermal conductance and resistance of the hot end copper sheet, $K_{h,cu}^j$ and $R_{h,cu}^j$, are expressed as

$$K_{h,cu}^j = \frac{\left(\theta_p + \theta_n + \varphi\right)\delta_{cu}\lambda_{cu}^j}{\ln r_{pn} - \ln r_{h,cu}} \tag{A.3}$$

$$R_{h,cu}^j = \frac{\left(\ln r_{pn} - \ln r_{h,cu}\right)\delta_{cu}\lambda_{cu}^j}{\theta_p + \theta_n + \varphi} \tag{A.4}$$

The thermal conductance and resistance of the cold end copper sheet, $K_{c,cu}^j$ and $R_{c,cu}^j$, are expressed as

$$K_{c,cu}^j = \frac{\left(\theta_p + \theta_n + \varphi\right)\delta_{cu}\lambda_{cu}^j}{\ln r_{cu} - \ln r(m)} \tag*{(A5)}$$

$$R_{c,cu}^j = \frac{\left[\ln r_{cu} - \ln r(m)\right]\delta_{cu}\lambda_{cu}^j}{\theta_p + \theta_n + \varphi} \tag{A.6}$$

The thermal conductance $K_{c,cer}^j$ of the cold end ceramic plate is

$$K_{c,cer}^j = \frac{4\pi\delta_{cer}\lambda_{cer}^j}{\ln r_{c,cer} - \ln r_{c,cu}} \tag{A.7}$$

Then the coefficients g_1, g_2, g_3, and g_4 are

$$g_1 = q\cdot K_{h,cu}^j\cdot R_{h,cu}^j + 0.5K_{h,cer}^j\cdot R_{h,cu}^j \tag{A.8}$$

$$g_2 = K_{h,cer}^j\cdot K_{h,cu}^j \Big/ \left(q\cdot K_{h,cu}^j + K_{h,cer}^j\right) \tag{A.9}$$

$$g_3 = 2K_{c,cer}^j\cdot K_{c,cu}^j \Big/ \left(2q\cdot K_{c,cu}^j + K_{c,cer}^j\right) \tag{A.10}$$

$$g_4 = R^j_{c,cu} \cdot K^j_{c,cer} \Big/ \left(2q \cdot K^j_{c,cu} + K^j_{c,cer}\right) + 2R^j_{c,cu} \tag{A.11}$$

References

[1] Y. Li, M. Vilathgamuwa, S.S. Choi, B. Xiong, J. Tang, Y. Su, Y. Wang, Design of minimum cost degradation-conscious lithium-ion battery energy storage system to achieve renewable power dispatchability, Appl. Energy 260 (2020), 114282.

[2] G. Fan, Y. Dai, Thermo-economic optimization and part-load analysis of the combined supercritical CO_2 and Kalina cycle, Energ. Convers. Manage. 245 (2021), 114572.

[3] H. Ghaebi, H. Rostamzadeh, Performance comparison of two new cogeneration systems for freshwater and power production based on organic Rankine and Kalina cycles driven by salinity-gradient solar pond, Renew. Energy 156 (2020) 748–767.

[4] Z. Yang, Y. Zhang, Q. Dong, J. Lin, G. Lin, J. Chen, Maximum power output and parametric choice criteria of a thermophotovoltaic cell driven by automobile exhaust, Renew. Energy 121 (2018) 28–35.

[5] E. Bellos, C. Tzivanidis, Incorporation of an organic Rankine cycle in a transcritical booster CO_2 refrigeration system, Int. J. Energy Res. 44 (2020) 7974–7988.

[6] A. Massaguer, T. Pujol, M. Comamala, E. Massaguer, Feasibility study on a vehicular thermoelectric generator coupled to an exhaust gas heater to improve aftertreatment's efficiency in cold-starts, Appl. Therm. Eng. 167 (2020), 114702.

[7] W. Yang, W. Zhu, Y. Yang, L. Huang, Y. Shi, C. Xie, Thermoelectric performance evaluation and optimization in a concentric annular thermoelectric generator under different cooling methods, Energies 15 (2022) 2231.

[8] X. Li, C. Xie, S. Quan, Y. Shi, Z. Tang, Optimization of Thermoelectric Modules' Number and Distribution Pattern in an Automotive Exhaust Thermoelectric Generator, IEEE Access 7 (2019) 72143–72157.

[9] M. Hekim, E. Cetin, Energy analysis of a geothermal power plant with thermoelectric energy harvester using waste heat, Int. J. Energy Res. 45 (15) (2021) 20891–20908.

[10] X. Li, C. Xie, S. Quan, L. Huang, W. Fang, Energy management strategy of thermoelectric generation for localized air conditioners in commercial vehicles based on 48 V electrical system, Appl. Energy 231 (2018) 887–900.

[11] X. Liu, Y.D. Deng, Z. Li, C.Q. Su, Performance analysis of a waste heat recovery thermoelectric generation system for automotive application, Energy Convers. Manag. 90 (2015) 121–127.

[12] R. Wang, W. Yu, X. Meng, Performance investigation and energy optimization of a thermoelectric generator for a mild hybrid vehicle, Energy 162 (2018) 1016–1028.

[13] Y. Jia, Z. Zhang, C. Wang, H. Sun, W. Zhang, Design and parameter study of a thermoelectric generator for waste heat recycling in flexible micro-light-emitting diodes, Appl. Therm. Eng. 200 (2022), 117568.

[14] Y. Cao, N.H. Abu-Hamdeh, H. Moria, S. Asaadi, R. Alsulami, A novel proposed flexible thin-film solar annular thermoelectric generator, Appl. Therm. Eng. 183 (2021), 116245.

[15] M. Ge, X. Wang, Y. Zhao, S. Wang, L. Liu, Performance analysis of vaporizer tube with thermoelectric generator applied to cold energy recovery of liquefied natural gas, Energ Convers Manage 200 (2019), 112112.

[16] Z.-G. Shen, S.-Y. Wu, L. Xiao, Theoretical analysis on the performance of annular thermoelectric couple, Energ. Convers. Manage. 89 (2015) 244–250.

[17] Z.-G. Shen, S.-Y. Wu, L. Xiao, Assessment of the performance of annular thermoelectric couples under constant heat flux condition, Energ. Convers. Manage. 150 (2017) 704–713.

[18] A.B. Zhang, B.L. Wang, D.D. Pang, J.B. Chen, J. Wang, J.K. Du, Influence of leg geometry configuration and contact resistance on the performance of annular thermoelectric generators, Energ. Convers. Manage. 166 (2018) 337–342.

[19] A.B. Zhang, B.L. Wang, D.D. Pang, L.W. He, J. Lou, J. Wang, J.K. Du, Effects of interface layers on the performance of annular thermoelectric generators, Energy 147 (2018) 612–620.

[20] S. Fan, Y. Gao, Numerical simulation on thermoelectric and mechanical performance of annular thermoelectric generator, Energy 150 (2018) 38–48.

[21] S, Asaadi, S, Khalilarya, S, SJafarmadar Numerical study on the thermal and electrical performance of an annular thermoelectric generator under pulsed heat power with different types of input functions. Energ Convers Manage 2018;167: 102–112.

[22] Y. Sun, G. Chen, B. Duan, G. Li, P. Zhai, An annular thermoelectric couple analytical model by considering temperature-dependent material properties and Thomson effect, Energy 187 (2019), 115922.

[23] Q. Tan, G. Chen, Y. Sun, B. Duan, G. Li, P. Zhai, Performance of annular thermoelectric couples by simultaneously considering interface layers and boundary conditions, Appl. Therm. Eng. 174 (2020), 115301.

[24] Y.-W. Gao, C.-L. Shi, X.-D. Wang, Numerical study on transient supercooling performance of annular thermoelectric cooler, Appl. Therm. Eng. 182 (2021), 116090.

[25] M.H. Zaher, M.Y. Adbelsalam, J.S. Cotton, Non-dimensional design optimization of annular thermoelectric generators integrated in waste heat recovery applications, Energ. Convers. Manage. 253 (2022), 115141.

[26] Z. Weng, F. Liu, W. Zhu, Y. Li, C. Xie, J. Deng, L. Huang, Performance improvement of variable-angle annular thermoelectric generators considering different boundary conditions, Appl. Energy 306 (2022), 118005.

[27] S. Fan, Y. Gao, Numerical analysis on the segmented annular thermoelectric generator for waste heat recovery, Energy 183 (2019) 35–47.

[28] S. Shittu, G. Li, X. Zhao, X. Ma, Y.G. Akhlaghi, E. Ayodele, High performance and thermal stress analysis of a segmented annular thermoelectric generator, Energ. Convers. Manage. 184 (2019) 180–193.

[29] S. Asaadi, S. Khalilarya, S. Jafarmadar, A thermodynamic and exergoeconomic numerical study of two-stage annular thermoelectric generator, Appl. Therm. Eng. 156 (2019) 371–381.

[30] M.-W. Tian, L.W.W. Mihardjo, H. Moria, S. Asaadi, H.S. Dizaji, S. Khalilarya, P. T. Nguyen, A comprehensive energy efficiency study of segmented annular thermoelectric generator; thermal, exergetic and economic analysis, Appl. Therm. Eng. 181 (2020), 115996.

[31] M. Aljaghtham, E. Celik, Numerical analysis of energy conversion efficiency and thermal reliability of novel, unileg segmented thermoelectric generation systems, Int. J. Energy Res. 45 (2021) 8810–8823.

[32] Y.J. Cui, B.L. Wang, K.F. Wang, L. Zheng, Power output evaluation of a porous annular thermoelectric generator for waste heat harvesting, Int. J. Heat Mass Transfer 137 (2019) 979–989.

[33] X.X. Tian, S. Asaadi, H. Moria, et al., Proposing tube-bundle arrangement of tubular thermoelectric module as a novel air cooler [J], Energy 208 (2020), 118428.

[34] W. Yang, W. Zhu, Y. Li, L. Zhang, B. Zhao, C. Xie, Y. Yan, L. Huang, Annular thermoelectric generator performance optimization analysis based on concentric annular heat exchanger, Energy 239 (2022), 122127.

[35] Y. Yang, S. Wang, Y. Zhu, Evaluation method for assessing heat transfer enhancement effect on performance improvement of thermoelectric generator systems, Appl. Energy 263 (2020), 114688.

[36] B. Huang, Z.-G. Shen, Performance assessment of annular thermoelectric generators for automobile exhaust waste heat recovery, Energy 246 (2022), 123375.

[37] C. Lai, Q. Zhao, Z. Zhang, H. Zhang, S. Hou, J. Zhao, Potential evaluation of flexible annular thermoelectric generator in photovoltaic system performance improvement: energy and exergy perspectives, Energ. Convers. Manage. 247 (2021), 114711.

[38] W, Zhu, Z, Weng, Y, Li, L, Zhang, B, Zhao, C, Xie, Y, Shi, L, Huang, Y,Yan, Theoretical analysis of shape factor on performance of annular thermoelectric generators under different thermal boundary conditions. Energy 239;2022:122285.

[39] Z.-G. Shen, B. Huang, X. Liu, Effect of structure parameters on the performance of an annular thermoelectric generator for automobile exhaust heat recovery, Energ. Convers. Manage. 256 (2022), 115381.

[40] M. Zhang, J. Wang, Y. Tian, Y. Zhou, J. Zhang, H. Xie, Z. Wu, W. Li, Y. Wang, Performance comparison of annular and flat-plate thermoelectric generators for cylindrical hot source, Energy Rep. 7 (2021) 413–420.

[41] W, Tao, S, Yang, Heat transfer. Fifth ed. Beijing: Higher Education Press; 2019.

[42] W. He, R. Guo, H. Takasu, Y. Kato, S. Wang, Performance optimization of common plate-type thermoelectric generator in vehicle exhaust power generation systems, Energy 175 (2019) 1153–1163.

[43] D. Luo, Z. Sun, R. Wang, Performance investigation of a thermoelectric generator system applied in automobile exhaust waste heat recovery, Energy 238 (2022), 121816.

[44] G. Yu, G. Shu, H. Tian, H. Wei, L. Liu, Simulation and thermodynamic analysis of a bottoming Organic Rankine Cycle (ORC) of diesel engine (DE), Energy 51 (2013) 281–290.

[45] O. Caballero-Calero, M. Rull-Bravo, D. Platzek, M.D. Cardenas, R. Fernandez, A. Moure, et al., Tubular ring thermoelectric module for exhaust pipes: from Skutterudite nanopowders to the final device, Energy 234 (2021), 121223.

[46] X. Niu, J. Yu, S. Wang, Experimental study on low-temperature waste heat thermoelectric generator, J. Power Sources 188 (2) (2009) 621–626.

[47] Y. Ge, Z. Liu, H. Sun, W. Liu, Optimal design of a segmented thermoelectric generator based on three-dimensional numerical simulation and multi-objective genetic algorithm, Energy 147 (2018) 1060–1069.

[48] W.-H. Chen, P.-H. Wu, Y.-L. Lin, Performance optimization of thermoelectric generators designed by multi-objective genetic algorithm, Appl. Energy 209 (2018) 211–223.

[49] Z. Liu, S. Zhu, Y. Ge, F. Shan, L. Zeng, W. Liu, Geometry optimization of two-stage thermoelectric generators using simplified conjugate-gradient method, Appl. Energy 190 (2017) 540–552.

[50] Y, Zhu, Newbrook DW, Dai P, Keed de groot CH, Huang R. Artificial neural network enabled accurate geometrical design and optimisation of thermoelectric generator. Appl Energy 2022;305:117800.

[51] J.-H. Meng, X.-X. Zhang, X.-D. Wang, Multi-objective and multi-parameter optimization of a thermoelectric generator module, Energy 71 (2014) 367–376.

[52] R. Arora, S.C. Kaushik, R. Arora, Multi-objective and multi-parameter optimization of two-stage thermoelectric generator in electrically series and parallel configurations through NSGA-II, Energy 91 (2015) 242–254.

[53] W. Zhu, W. Yang, Y. Yang, Y. Li, H. Li, Y. Shi, Y. Yan, C. Xie, Economic configuration optimization of onboard annual thermoelectric generators under multiple operating conditions, Renew. Energy 197 (2022) 486–499.

[54] L. Zhu, H. Li, S. Chen, X. Tian, X. Kang, X. Jiang, S. Qiu, Optimization analysis of a segmented thermoelectric generator based on genetic algorithm, Renew. Energy 156 (2020) 710–718.

[55] D. Luo, R. Wang, Y. Yan, Z. Sun, W. Zhou, R. Ding, Comparison of different fluid-thermal-electric multiphysics modeling approaches for thermoelectric generator systems, Renew. Energy 180 (2021) 1266–1277.